Ensembles of Multiple Models for Soil Moisture Retrieval from Remote Sensing Data over Agricultural Areas: A Deep Learning-based Framework

Amir Sedighi[1], Saeid Hamzeh[1 *], Seyed Kazem Alavipanah[1], Abd Ali Naseri[2], Peter M. Atkinson[3]

[1] Department of Remote sensing & GIS, Faculty of Geography, University of Tehran, Tehran, Iran, amir.sedighi@ut.ac.ir, saeid.hamzeh@ut.ac.ir, salavipa@ut.ac.ir

[2] Department of Irrigation and Drainage, Faculty of Water Sciences Eng., Shahid Chamran University of Ahvaz, Ahvaz, Iran, abdalinaseri@scu.ac.ir

[3] Lancaster Environment Center, Lancaster University, Bailrigg, Lancaster LA1 4YW, UK, pma@lancaster.ac.uk

* Corresponding author E-mail: saeid.hamzeh@ut.ac.ir

Ensembles of Multiple Models for Soil Moisture Retrieval from Remote Sensing Data over Agricultural Areas: A Deep Learning-based Framework

Abstract

In agricultural areas, most surface soil moisture (SM) retrieval models are unstable in terms of their accuracy and performance during crop growth. As a result, there is no consensus on which model performs optimally during the agricultural season. This is because of the uncertainties associated with model physics, initial conditions, model inversion processes, input data, vegetation attenuation and soil characteristics. To better deal with these practical concerns, we propose a simple, but robust SM retrieval method of using combination of multiple models based on deep learning and multi-model ensemble approach, called the DL-MME method, which makes use of the 'collective intelligence' and 'wisdom of crowds' concepts. The advantages of this method are: (1) robustness to model selection, and (2) robustness to model calibration during the growing season. In addition, this method is less dependent on one type of data across various agricultural areas compared to the single model approach. Firstly, the coupled water cloud model (WCM) and soil backscattering models (Oh model or advanced integral equation model (AIEM)) with different vegetation descriptors were calibrated and validated during the growing season in sugarcane and winter wheat fields for Sentinel-1 backscattering coefficients (VV and VH). SM was also retrieved by employing the trapezoid model (OPTRAM) with different parameters from Sentinel-2 images. To optimize SM retrieval computations, we used the outputs from optical and SAR models, auxiliary features, and reliable in situ SM measurements as inputs to a deep learning convolutional neural network (DL-CNN). For sugarcane and wheat fields in the early stages of crop growth, WCM models retrieved more accurate time-series SM than optical models. OPTRAM soil moisture retrievals showed greater accuracy in the late crop growing season. Time-series SM retrieval accuracy using DL-MME was higher than for the optical and semi-empirical SAR models. According to the results of the *in situ* validation for wheat (sugarcane) fields, the minimum MAE by an optimal combination of models was around 0.01 (0.02) m^3m^{-3} (RMSE= 0.036 (0.074) m^3m^{-3}; R= 0.87 (0.71)). The findings demonstrate that our method is reliable and feasible for SM retrieval. Additionally, our method provides a way to select an optimal model for retrieving time-series SM during the crop growing season.

Keywords: Soil moisture, Agriculture, Multi-model, Deep learning, Remote sensing.

1. Introduction

Surface soil moisture (SM) monitoring over different areas is a challenging task, and considerable improvements have been made in methodology over several decades leading to a large number of operational applications. Satellite observations provide advantages such as real-time, low cost and high efficiency which make them particularly effective for monitoring time-series SM (Fathololoumi et al. 2020; Liu et al. 2019). Accurate SM information plays a significant role in agricultural applications, such as irrigation scheduling (Domínguez-Niño et al. 2020), crop water demand identification (Singh and Das 2022), yield prediction (Champagne et al. 2019) and drought monitoring (Martínez-Fernández et al. 2016). Such information can facilitate irrigation-efficient agriculture and help ensure food security, particularly in areas with arid and semi-arid conditions.

Over the past few decades, technological advances in remote sensing have enabled the spatial time-series SM monitoring from optical, thermal infrared (TIR) and microwave (passive and active) observations (Barrett et al. 2009; Zhang and Zhou 2016). More recently, novel approaches and algorithms were developed to retrieve SM using satellite-based optical/TIR or optical/microwave observations in synergy. Although TIR and passive microwave data are useful for providing SM information at regional and global levels, their coarse spatial and temporal resolutions prevent them from providing data for retrieval of time-series SM in agricultural areas (Ebrahimi-Khusfi et al. 2018; Khazaei et al. 2023; Petropoulos et al. 2015).To estimate SM content, several types of optical models were used, including empirical, semi-empirical and physically-based models. However, optical models have three main limitations (cloudy sky, shallow measurement depth and calibration of empirical methods). Nevertheless, some physical models were demonstrated to overcome the limitations of empirical methods in terms of calibration, thus, facilitating universal parameterization with great potential for agricultural applications (Ambrosone et al. 2020; Foroughi et al. 2020). Sadeghi et al. (2017) proposed a novel trapezoidal model based on physical principles, OPtical TRApezoid Model (OPTRAM), suitable for vegetated areas.

With active microwave observations (e.g. synthetic aperture radar (SAR) sensors), time-series SM can be retrieved under all weather conditions with fine spatial resolution, ideal for field-based applications (Zeyliger et al. 2022). However, soil surface roughness and vegetation have an impact on active signals (Moran et al. 2004). SAR backscattering coefficients have been related to SM content on surfaces that are barren or sparsely vegetated using physical (such as the integral equation model (IEM) or advanced IEM (AIEM) model), empirical, and semi-empirical models (such as Dubois model and Oh model) (Chen et al. 2003; Dubois et al. 1995; Fung et al. 1992; Oh 2004). The majority of the above-mentioned models are based on bare soil. However, SM under a vegetated canopy can be retrieved by coupling a SAR vegetation scattering model with a soil backscattering model. Both the water cloud model (WCM) (Attema and Ulaby 1978) and the Michigan microwave canopy scattering (MIMICS) model (Ulaby et al. 1990) were developed to deal with homogeneous and dense vegetation surfaces. these methods have been implemented for several crops (Ayari et al. 2022; Bousbih et al. 2018; Wu et al. 2020). As far as agricultural applications are concerned, the majority of surfaces are covered by some degree of vegetation. Dielectric characteristics, as well as vegetation structure, play an important role in attenuating or affecting SAR backscattering (Ulaby et al. 1982). The synergy between optical and SAR data, in particular, is useful for the separation of surface roughness and vegetation biomass effects on SAR backscattering coefficients to improve the retrieval of SM (Petropoulos et al. 2020; Rawat et al. 2019; Wang et al. 2020).

The retrieval of soil parameters has been improved significantly over traditional models in the last few years as deep learning methods have been employed progressively (Gao et al. 2022;

Ge et al. 2018; Leng et al. 2023; Zhang et al. 2022). A deep learning-based Unsupervised Self-Training Method (USTM) was employed by Ben Abbes and Jarray (2022) to estimate SM using the normalized difference infrared index (NDII) and normalized difference vegetation index (NDVI) from S-2A, backscatter coefficients from S-1A and *in situ* data. Compared to other methods, USTM based on random forest (RF) and convolutional neural networks (CNN) provided the highest precision and accuracy. In remote sensing applications, deep learning neural networks (DL-NN) are particularly useful when the physical models of the problem are highly complex (e.g., ill-posed inverse problems, nonlinear relationships and non-generalizability) (Yuan et al. 2020). Currently, optical, TIR and SAR observations can be utilized to obtain reliable time-series SM information that can meet the requirements of agricultural applications. Specific requirements consist of full geographic coverage, fine spatial resolution (less than 100 m^2), time-series recording (weekly observation cycles), and sufficient accuracy (ubRMSE below 0.04 m^3m^{-3}) (Li et al. 2021; Peng et al. 2021). When SM retrieval models are applied in practice, investigators are commonly faced with three basic problems: (1) which model should be selected among the available models, and (2) what is the appropriate calibration, and perhaps more challenging, (3) when should each model be applied during the crop growing season?

To the best of our knowledge, no general agreement exists on which model performs optimally during the agricultural season. This is due mainly to the uncertainties associated with model physics, initial conditions, the assumptions made, model inversion processes, input data, vegetation attenuation effects, different representations of canopy aerodynamics and varying soil characteristics. A comprehensive review of the available models is needed to answer the first question, as there is no clear guide to selecting SM retrieval models for various agricultural areas. A second problem arises when multiple users utilize the same fundamental model, but with different calibrations, which may lead to inconsistent results. In many cases, the calibration predefined by the original model developers needs to be re-calibrated for each region. For the third question it is important to consider the availability of satellite sensor data as well as crop conditions at different dates during the growing season. At different dates of the crop growing season, effective parameters for SM content can change dramatically, making the accuracy and efficiency of a single model potentially sub-optimal. Over the past few years, alternative solutions have been explored, such as new models that are robust and relatively insensitive to calibration processes. This can be done by either developing new approaches or by utilizing multiple existing models as the basis for novel approaches. The latter approach is generally favoured because the combination of multiple models can achieve synergies based on the merits of each. These approaches borrow from the concepts of 'collective intelligence' (Malone et al. 2009) and 'wisdom of crowds' (Surowiecki 2005), where multiple models can provide complementary information to support more accurate and reliable prediction than each model individually.

Inspired by these ideas, we propose a novel method to address the three above-mentioned challenges for effective time-series SM retrieval. The proposed method is based on a deep learning framework to exploit the advantages of individual SM retrieval models in combination. The advantages of this novel method are: (1) robustness to model selection, and (2) robustness to model calibration during the growth season. In addition, this method is less dependent on one type of data across various agricultural areas compared to the single model approach. The proposed framework is essentially a simple, but effective ensemble approach, referred to as Deep Learning-based Multi-Model Ensemble (DL-MME). The DL-MME method combines SAR and optical models for the first time for SM retrieval. Importantly, the proposed method combines multiple models, which differs from earlier studies that focused on the combination and synergistic use of different spectral data.

2. Study area and Data

2.1. Study area

In this research to test the effectiveness of DL-MME, fields of two types of crops (sugarcane and wheat) with different scattering mechanisms and growth patterns were selected as study sites. A key criterion in selecting these fields for this research was the availability of *in situ* data (especially surface roughness parameters) collected periodically during the crop growing season. In agricultural fields, it is difficult to obtain sufficient quantities or quality of *in situ* data for remotely sensed SM models.

2.1.1 Sugarcane fields

Sugarcane fields of Amirkabir sugarcane Agro-industry Company in the Khuzestan province, Iran, located approximately 50 km southwest of Ahwaz city, were selected as one of the study sites (Fig. 1a). An area of approximately 9,200 ha was under study in 2020, out of a total of 12,000 ha. The sugarcane fields of the region are generally homogenous and extend to 25 hectares (1000x250 m). This region has a semi-arid climate with 266 mm of average annual rainfall. In July the average maximum monthly temperature is 38°C and in January the average minimum monthly temperature is 12.4°C. According to estimates, the reference evapotranspiration (ET_0) rate is approximately 3330 mm per year. The soil texture in most fields is typically clay loam and silty clay loam. Monitoring of sugarcane fields was conducted during the growth season of 2020. Similar irrigation management, drainage systems, and operational practices are employed in the study area.

2.1.2. Wheat fields

Three irrigation fields (F1 to F3) in the Chichaoua Province of Marrakesh-Safi Region, Morocco, located approximately 17 km southeast of Chichaoua city, were selected as the study sites (Fig. 1b). This region has a semi-arid Mediterranean climate with 250 mm of average annual rainfall. In July-to-August the average maximum monthly temperature is 27.2°C and in January the average minimum monthly temperature is 10.8°C. According to estimates, the reference evapotranspiration (ET_0) rate is approximately 1600 mm per year. Monitoring of F1 and F2 (each approximately 1.5 ha) was conducted over two consecutive growth seasons (2016-2017; 2017-2018), and monitoring of F3 (about 12 ha) was undertaken during the growth season of 2018-2019. The soil texture in these fields is typically loamy-clay (32.5% sand, 37.5% clay). They are irrigated by drip irrigation and the wheat crop is cultivated once each year in the winter and spring in all the fields (Ouaadi et al. 2021).

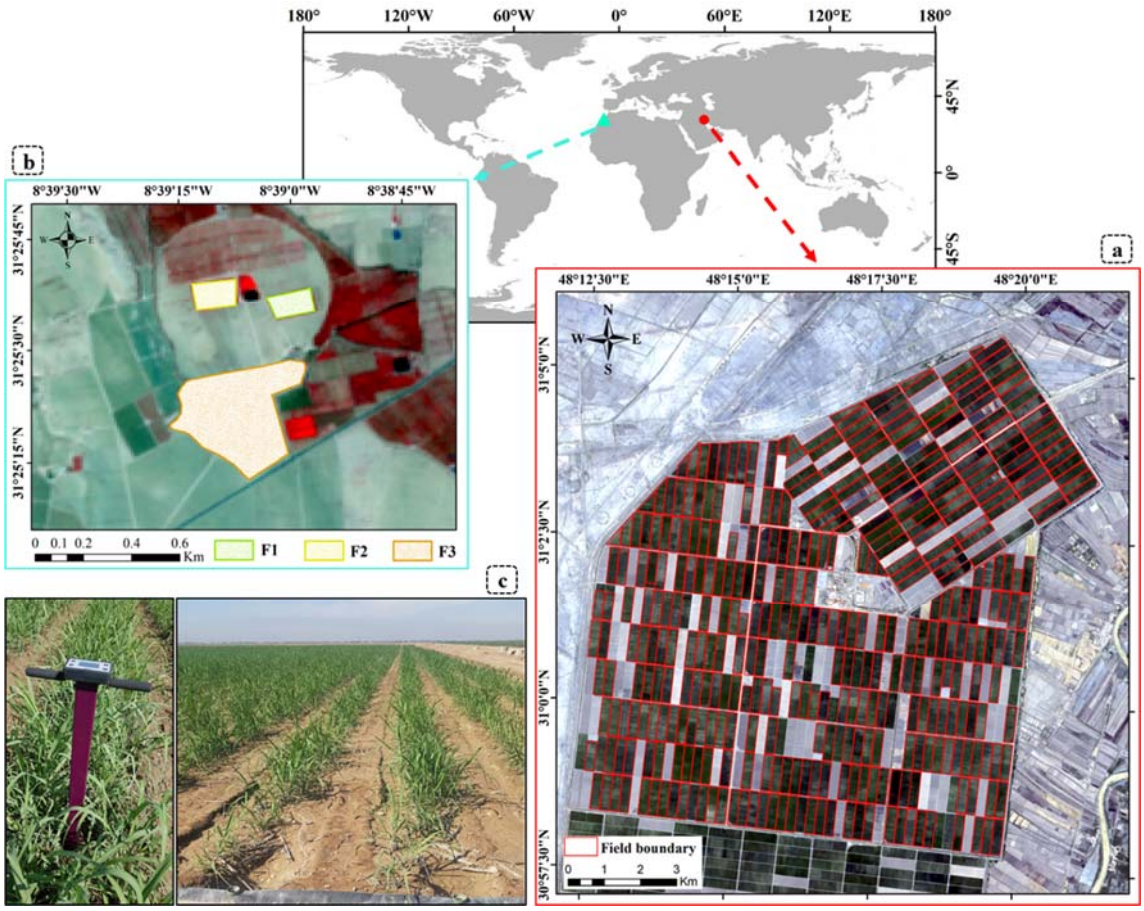

Figure 1. Location of the study areas: (a) Sugarcane fields and (b) Wheat fields. (c) Field sampling with a Fieldscout TDR 350 soil moisture meter.

2.2. Data

2.2.1. Field measured data

Two main groups of measurements were acquired in this research: soil measurements (surface roughness and surface soil moisture) and crop measurements (crop height (H_c), fractional vegetation cover (FVC), leaf area index (LAI), vegetation water content (VWC), fresh above-ground biomass (FAGB), and above-ground biomass (AGB)).

A time-series of half-hourly SM was automatically measured in 60 sugarcane fields and 3 wheat fields with time domain reflectometry (TDR) sensors installed at a depth of 5 cm. Additionally, a Fieldscout TDR 350 soil moisture meter (Fig. 1c) was used for random sampling from other sugarcane fields concurrent with the Sentinel overpass during the growing season. As part of the first stages of crop growth, soil roughness was measured once a week until the crop canopy restricted further measurements. The soil roughness parameters describe the statistical variation in the height of the soil surface in relation to a reference surface (Verhoest et al. 2008). Based on the correlation functions of the surface heights, two parameters were calculated for each roughness profile: the correlation length (l) and the root mean square surface height (s). In each field, and for each date, an average l and s value was calculated based on 16 samples. FAGB measurements were taken about every two weeks throughout the growing season and weighed immediately. After drying, samples are weighed to calculate the AGB (kg DM m^{-2}). Based on the difference between the wet and dry samples, VWC was calculated. Also, weekly measurements of H_c, LAI, and FVC were obtained throughout the growing season. In the measurement of H_c, values are taken from various points in each field

and averaged. The LAI and FVC were calculated using the hemispherical photography method based on an average of eight photos per date and field. The FVC was calculated as the ratio of vegetation pixels to the total pixels.

Irrigation data (quantities and dates) were available for sugarcane fields and wheat fields (F1 and F2, but not F3). An automatic weather station collected continuous weather data every 30 min, including precipitation, air temperature, relative humidity, solar radiation and wind speed. More details about wheat fields data, measurements and collection methods can be obtained from Ouaadi et al. (2021).

2.2.2. Remote sensing data

During the study period, the Sentinel-1 satellites (S-1A and S-1B) provided C-band SAR images at least once a week for the study sites. Most commonly used is the IW (Interferometric Wide-swath) mode, which contains dual polarizations (VH and VV). The range and azimuth resolutions of the data are 5 m and 20 m. Ground Range Detected (GRD) products are available from the European Space Agency (ESA). Between February and November 2020 (one agricultural season), 72 GRD products were available for sugarcane fields. In the case of wheat fields, between October 2016 and July 2018 (two agricultural seasons), 207 GRD products were available for F1 and F2, while 65 products were available for F3 from November 2018 until May 2019 (one agricultural season). In this research, the backscattering coefficients of these products were used to extract SAR features, compare surface backscattering models and, ultimately, retrieve SM.

The Sentinel-2 satellites (S-2A and S-2B) provide images in 13 bands (with spatial resolutions of 10 to 60 m) at least once a week for the study sites. S-2 Level-1C (L1C) products are also available from ESA. The L1C data are Top-Of-Atmosphere (TOA) reflectance products, which require atmospheric correction to calculate surface reflectance. Over sugarcane fields, 90 out of 144 S-2A available images for the 2020 crop season were cloudless. Over F1 and F2 (wheat fields), 10 out of 17 S-2A available images for the first crop season and 25 out of 33 S-2A available images for the second crop season were cloudless. Over F3, 27 out of 39 S-2A available images for the 2018-2019 crop season were cloudless. The S-2 images were employed to obtain spectral (vegetation and water) indices, biophysical variables and optical SM models.

3. Methods

3.1. The rationale underpinning the DL-MME method

An innovative method of using SAR and optical models for time-series SM retrieval is proposed to address the basic problems of SM retrieval over agricultural areas during the crop growing season. The DL-MME method combines a group of SAR backscattering and optical models to provide more accurate and stable SM retrievals at different dates. The logic behind DL-MME is that a group of models can complement one another to provide enhanced information compared to a single model, in accordance with the ‘collective intelligence’ and ‘wisdom of crowds’ concepts. It is defined as collective intelligence when groups of individuals behave in a manner that appears intelligent (Malone et al. 2009). With their knowledge, different individuals can present different approaches and viewpoints, leading to a more appropriate solution or interpretation of a specific problem (Leimeister 2010). In line with the collective intelligence paradigm, this research focused on the use of groups of models to increase accuracy and performance over an individual using them alone.

However, estimates based on multi-model ensembles are not guaranteed to be better than individual estimates. When selecting models, it is important to know when to trust ensembles and when to be cautious. A carefully constructed ensemble is crucial, and simply adding different models is not sufficient (Stumpf 2020). For some problems, model selection may be unable to determine the most appropriate model. There may be many models with comparable support, in which case estimates might then be made using an ensemble of models supported by the available data. The relative contribution of each model to the estimation process is weighted according to its relative support. This method is often referred to as taking advantage of the 'wisdom of crowds' (Marbach et al. 2012; Surowiecki 2005). An ensemble of carefully selected models will generally be more accurate than methods relying on one model. DL-MME can provide a comprehensive solution for time-series SM retrieval by selecting models and achieving stable accuracy under different conditions. An overview of the step-by-step process of DL-MME can be found in Fig. 2.

Firstly, the S-1 and S-2 images were preprocessed to obtain backscattering coefficients (VH and VV) and S-2 L2A products. In the following step, the preprocessed satellite sensor images were used to extract various features. The Sentinel-2 L2A bands were used to calculate optical features such as NDVI, LAI and FVC. In addition, SAR backscattering coefficients were used to extract a range of SAR features such as radar vegetation index (RVI), incidence angle (θ), polarization ratio (PR), and polarization difference. Interpretation of the time-series of backscattering coefficients and vegetation descriptors, as well as their relationship with SM, was undertaken to determine the impact of each parameter on models at various stages of the growing season. A third step involved calibrating and validating the coupled WCM and soil backscattering models (Oh or AIEM) for S-1 backscattering coefficients (VV and VH) during the growing season in fields based on different vegetation descriptors. Different parameterizations of OPTRAM were employed from the S-2 images to retrieve SM. Following this, a moderator was employed as an adjudicator. The role of a moderator is to pre-select the models based on predetermined rules. As part of the fourth step, parametrized optical models, calibrated SAR models, features and reliable *in situ* SM measurements were used to create training and test datasets, and then a deep learning convolutional neural network (DL-CNN) was used to combine the multiple models and approximate SM by optimal computation. As a final step, the DL-MME results were assessed for accuracy by performing *in situ* SM measurements. Additionally, the retrieval results were compared with single optical and SAR models.

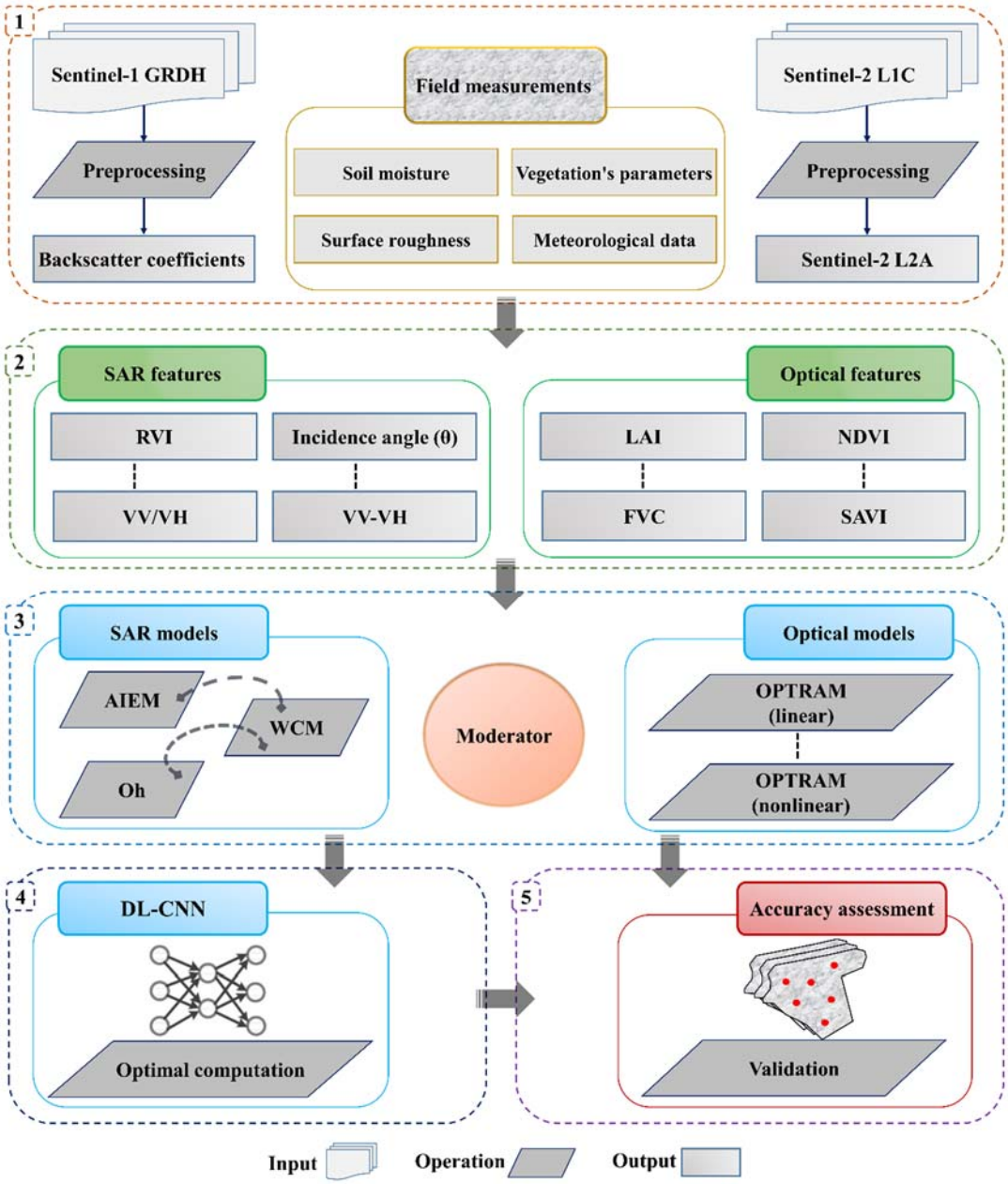

Figure 2. The DL-MME workflow.

3.2. Data preprocessing and feature extraction

Preprocessing the S-1 images included applying Orbit File, thermal noise removal, radiation calibration, speckle reduction (multi-look), range Doppler terrain correction and decibel (dB) conversion (Moskolaï et al. 2022). Then, images of the backscattering coefficients (σ°_{VV} and σ°_{VH}) were obtained at a spatial resolution of 20 m. Through the Sen2Cor plug-in of the Sentinel application platform (SNAP), S-2 L2A was derived from S-2 L1C. The spatial resolution of all surface reflectance bands was resampled to 20 m. The biological quantity module in SNAP was used to calculate the FVC, LAI, fraction of absorbed photosynthetically active radiation (FAPAR), canopy chlorophyll content (CCC) and canopy water content (CWC) parameters. This module estimates these parameters based on the PROSAIL radiative transfer model, a combined model of PROSPECT (leaf reflectance and transmittance) and SAIL (plant canopy reflectance), and an artificial neural network (ANN) (Hu et al. 2020; Weiss et al. 2020).

3.3. SAR backscattering models

The SAR backscattering coefficients are generally influenced by SM content and surface roughness in bare soil areas. Plant growth may complicate SM retrieval in vegetated areas (Autret et al. 1989; Brogioni et al. 2010). Semi-empirical WCM is designed to simulate radar backscatter over the canopy of vegetation. In fact, the dielectric constant of vegetative matter is considerably smaller than those of water, and the canopy of vegetation is typically composed of at least 99% air by volume. So the vegetation canopy in WCM is considered a cloud of water droplets that are held in place by vegetative matter. (Attema and Ulaby 1978).

Basically, the WCM assumes: (1) it is possible to ignore multiple scattering inside the canopy volume; (2) cloud density and height are closely related to the VWC parameter. The WCM is valid for frequencies ranging from 8 to 18 GHz and incidence angles ranging from 0 to 70°. A simplified method was used to calculate the total σ° without taking into account multiple scattering within the canopy and soil (Pierdicca et al. 2010). It is therefore equivalent to the first-order solution to the radiative transfer equation in a weak medium. As a result, canopy backscattering coefficients are calculated incoherently from three contributions (Eq.1): volume scattering from vegetation (σ°_{veg}), attenuated surface scattering from the underlying soil (σ°_{soil}), and multiple scattering interactions between the soil and vegetation ($\sigma^{\circ}_{soil*veg}$).

$$\sigma^{\circ}_{canopy} = \sigma^{\circ}_{veg} + \tau^2 \ \sigma^{\circ}_{soil} \ + \ \sigma^{\circ}_{soil*veg} \tag{1}$$

$$\sigma^{\circ}_{veg} = A * V_1 + \cos\theta \, (1 - \tau^2) \tag{2}$$

$$\tau^2 = \ \mathrm{e}^{-2B \, V_2 / cos\theta} \tag{3}$$

where τ^2 is the canopy's two-way transmissivity factor and θ is the radar incidence angle. The A coefficient represents the direct scattering of vegetation, whereas the B coefficient corresponds to the attenuation of the underlying soil backscattering caused by the vegetation canopy. These coefficients are dependent on the type of canopy, the sensor's polarization and frequency, as well as the incidence angle. V_1 and V_2 are vegetation descriptors that describe the dynamics of the vegetation canopy (El Hajj et al. 2016; Ouaadi et al. 2020).

VWC was used to quantify the impacts of vegetation on backscatter coefficients in numerous radar vegetation models. Due to the direct relationship between VWC and radar penetration depth, VWC influences the quality of SM retrieval. To estimate the VWC, optical indices such as LAI, NDVI and the normalized difference water index (NDWI) are frequently employed (Baghdadi et al. 2017; Bai et al. 2017; Bao et al. 2018; Wang et al. 2020). This research utilized the Oh (Oh et al. 1992) and AIEM (Baghdadi et al. 2006) models to calculate the contribution of the soil component (σ°_{soil}) to WCM. The validity of these models was demonstrated for a broad range of incidence angles and soil roughness levels (Frison et al. 1998).

3.4. Optical models

In optical models, vegetation conditions are generally represented by optical bands or indices that are capable of relating them to SM in order to estimate SM indirectly over vegetated areas. In addition, vegetation has a self-adaptation function that is capable of adapting to SM changes within a short period of time, so there is expected to be a delay when using indices to infer SM conditions directly. With its simple trapezoidal design in short wave infrared (SWIR) bands and physically determinable parameters, OPTRAM provides a simple procedure for retrieving SM from optical data (Sadeghi et al. 2015). We selected this model because of its feasibility and potential for universal calibration across a wide range of soil types. Relative SM is estimated using Eq.4 by OPTRAM (Sadeghi et al. 2017).

$$W = \frac{\theta - \theta_d}{\theta_w - \theta_d} = \frac{STR - STR_d}{STR_W - STR_d} \quad (4)$$

where W is the relative or normalized SM content (0 for dry soil and 1 for saturated soil), and θ_d and θ_w are the local minimum dry SM content and the local maximum wet SM content (m3/m3), respectively. STR is the SWIR-transformed reflectance calculated according to Eq.5.

$$STR = \frac{(1 - R_{SWIR})^2}{2R_{SWIR}} \quad (5)$$

where R_{SWIR} is the SWIR reflectance. Two assumptions are used to develop the OPTRAM model: (1) the trapezoidal shape is determined by plotting STR against vegetation indices (VIs), which can either be NDVI or SAVI, and (2) STR and VI are linearly related along the lower (dry) and upper (wet) edges of the trapezoid. On the basis of the original OPTRAM (L-OPTRAM) of Sadeghi et al. (2017), the STR_d and STR_W parameters can be derived by assuming that soil water content is linearly related to vegetation water content (Eq. 6 and 7), and form the wet and dry edges of the STR-VI trapezoidal space.

$$STR_d = i_d + s_d VI \quad (6)$$
$$STR_w = i_w + s_w VI \quad (7)$$

where STR_d and STR_w are the STR at θ_d and θ_w, respectively. In the dry edge, i_d and s_d represent the intercept and slope, respectively, while in the wet edge, i_w and s_w are the intercept and slope, respectively. Several studies indicated, however, that the distribution of pixels within the STR-VI space of OPTRAM may not resemble perfectly a trapezoid, and that the correlation between VI and STR might be nonlinear at the edges, particularly when vegetation cover is high (Babaeian et al. 2018; Hassanpour et al. 2020; Mananze et al. 2019). According to Ambrosone et al. (2020), the wet and dry edges in STR-VI space exhibit a nonlinear trend, and so the nonlinear OPTRAM model (NL-OPTRAM) was proposed to retrieve the STR_d and STR_W parameters based on exponential functions (Eq. 8 and 9).

$$STR_d = i_d \, exp\,(s_d VI) \quad (8)$$
$$STR_w = i_w \, exp\,(s_w VI) \quad (9)$$

Model parameterization (calculation of the i_d, s_d, i_w and s_w parameters) is a crucial step in OPTRAM for obtaining reliable SM content (Babaeian et al. 2018). To parameterize OPTRAM, the pixels in each field were distributed in STR-VI space. Since STR and VI are subject to temporal variability, the STR-VI space based on one date is insufficient to parameterize the wet and dry edges (Chen et al. 2020; Ma et al. 2022).

For sugarcane (wheat) fields, the STR-VI spaces were derived using spectral indices (NDVI, SAVI, and LAI) based on two parameterization approaches (linear and nonlinear). All pixels of fields from S-2 time-series images over each season were extracted to create a STR-VI space covering a variety of SM conditions and growth stages throughout the crop growing season. To identify the appropriate parameterizations at different crop growth stages, it was necessary to compare the stability of model accuracy of different parameterized OPTRAM models for time-series SM retrieval and analyze the differences in their STR-VI space time-series. The STR-VI space time-series represents a series of single-date STR-VI spaces over the growing season.

To reduce computational cost and improve DL-MME performance, the moderator was used as a regulator parameter to preselect the optical and SAR models at each stage of the crop

growing season. DL-MME may not use all the available models (or features) during the growing season for a variety of reasons, including lack of access to a satellite sensor image on the desired date, weather conditions and a model's very low retrieval accuracy compared to other models (based on the mean and standard deviation of the models' accuracy). The moderator is actually a decision tree classifier that operates based on predetermined rules such as meteorological conditions (cloud cover percentage, precipitation events), vegetation cover percentage, scattering mechanisms and crop growth stage. At each date of the growing season, the moderator determines the minimum acceptable level of models. The moderator prevents the model from contributing to DL-MME if the level is not acceptable; if the level is acceptable, the moderator adopts a selection process to contribute the model to DL-MME.

3.5. DL-CNN algorithm for optimal computation

To optimize the DL-MME computation and select the optimal combination of models during the wheat growth season, deep learning neural networks were used. There are two factors that can be used to classify neural networks: their learning style and their network structure. A deep learning convolutional neural network (DL-CNN), characterized by a feedback network structure and supervised learning style, was chosen for this research. DL-CNN, like other neural networks, has the following common advantages: information extraction from training samples, instance-based feature exploration and discovery, simplifying physical model complexity and converting feature extraction to automated feature learning (LeCun et al. 2015; Liu et al. 2017). There are, however, several distinct advantages to DL-CNN, including its capability to decrease the number of parameters, its high fault-tolerance, its ability to run parallel computations, and its self-evaluation ability. Due to this, the method has high computational efficiency for parameter retrieval (Ge et al. 2018; Wang et al. 2021a).

Each basic unit of DL-CNN may consist of several operational layers such as convolution, pooling (sub-sampling), fully connected, and activation layers that are arranged between the input and output layers. Convolution and pooling operations are primarily used in DL-CNN for extracting relevant features from both the input and hidden layers, as well as extracting information from the data through shared weights and local connections (Molinier et al. 2021). To implement the convolution operation on the input data, multiple local filters (kernels) were used in the convolution layer. In the pooling layer, low-dimensional data can be obtained via several operations, including average-pooling and max-pooling. DL-CNN integrates pooling after convolution to reduce data amounts to minimize calculations and speed up training. Each pooling layer is interconnected with the previous convolution layer, enabling it to reduce the resolution of feature maps to guarantee invariance. DL-CNN can perform nonlinear fitting due to nonlinear operations at the activation layer. The label data and the output data share identical dimensions. This series of shrink operations should allow the output data and the label data to be as close to each other as possible (Yamashita et al. 2018; Yuan et al. 2020).

The arrangement of one neuron, consisting of the sum ($X \cdot W + b$) is often referred to as the neuron's net. W is the weight and b is the bias. There are two types of inputs to neurons: actual inputs (X) and outputs from neurons in the previous layers. There are several activation functions available, but the rectified linear unit (ReLU) function was used in this research. One of the main advantages of ReLU is its lower computational load (Alzubaidi et al. 2021). The neural network operates through a group of neurons trained to respond appropriately to inputs. The training phase involves presenting training patterns sequentially to the network and then adjusting the weights of each neuron in the network according to the training patterns. To achieve the learning objective, the mean square error in training must be minimized. The DL-CNN constructed in this research is based on Kalman filtering. It is a recursive method to

minimize the mean squared error (loss function) between the actual and estimated values. It significantly increases the DL-CNN's accuracy, training speed and stability. Further details can be found in Grewal and Andrews (2014).

DL-CNN training is generally straightforward, but hyperparameter tuning can be one of the most effective solutions to improve DL-CNN performance (Alzubaidi et al. 2021). Only the kernels are learned automatically during training rather than the hyperparameters which are set prior to training (Yamashita et al. 2018). Three key hyperparameters for DL-CNN should be set before the training process, namely the batch size (ω), learning rate (α), and number of convolutional layers (ι). The different sets for each hyperparameter are evaluated.

3.5.1. DL-CNN feature selection

A description of the features used in DL-CNN is provided in Table 1. The outputs of SAR and optical models are included in Group (A). Spectral indices, as well as biomass features (FVC, LAI, FAPAR, CCC and CWC), are included in Group (B). SAR features (PR, VV-VH, RVI and θ) are included in Group (C). Four configurations of these basic Groups (A to C) are then considered as inputs for DL-CNN. Configuration (D) consists only of Group (A). Configuration (E) consists of Groups (A) and (B). Configuration (F) consists of Groups (A) and (C). Configuration (G) consists of groups (A-C). Configuration (H) consists of Groups (B) and (C).

Table 1. Features used in DL-CNN for SM retrieval.

Group		Features
A		SAR ($\mathrm{WCM-Oh}_{NDVI}$, $\mathrm{WCM-Oh}_{VWC}$, $\mathrm{WCM-AIEM}_{NDVI}$, $\mathrm{WCM-AIEM}_{VWC}$, …) and optical ($\mathrm{OPTRAM}_{\mathrm{linear}}$, $\mathrm{OPTRAM}_{\mathrm{nonlinear}}$, …) models.
B		Optical features: Vegetation indices (NDVI, DVI (Tucker 1979), EVI, SAVI (Huete 1988), MSAVI (Qi et al. 1994)), water indices (NDWI (Gao 1996), MNDWI (Xu 2006)), and biomass features (FVC, LAI, FAPAR, CCC, and CWC) (Weiss et al. 2020).
C		SAR features: θ,VV-VH, PR, and RVI (Kim and van Zyl 2009).
Configuration	**D**	Models (A).
	E	Models and optical features (A and B).
	F	Models and SAR features (A and C).
	G	Models, optical and SAR features (A, B and C).
	H	Optical and SAR features (B and C).

3.6. Accuracy assessment

In situ data were used to evaluate the accuracy of the proposed method in actual applications. Three subsets of data were selected randomly from the available data (5500 samples for sugarcane crop and 1500 samples for wheat crop): a training subset (50%), a validation subset (20%), and a test subset (30%). For the purpose of avoiding dependency on the retrieval results of the sampling process, the dataset was sampled randomly five times. The CNN algorithm was trained based on a training subset, and the validation subset was used to evaluate the model during the training phase, fine-tune the hyperparameters and select the model. To assess the performance of the fine-tuned model independently, the completely unused test subset was employed only once at the final step of accuracy assessment (Santi et al. 2016; Yamashita et al. 2018). It should be noted that the CNN algorithm was implemented for each crop type separately. The accuracy of all SM retrieval models was evaluated using Pearson's correlation coefficient (R), the mean absolute error (MAE), and RMSE (Entekhabi et al. 2010; Rawat et al. 2019).

4. Results

In the first section of results, a time-series interpretation of backscattering coefficients and vegetation descriptors is presented based on crop growth stages during the agricultural season. The second section focuses on OPTRAM parameterization and WCM calibration, while the third section discusses SM retrieval based on DL-MME.

4.1. Time-series interpretation

The time-series of S-1 backscattering coefficients (VV and VH) at 43.5° (ascending orbit) and 37.8° (descending orbit) incidence angles, NDVI, NDWI and STR from S-2 and *in situ* measurements at different sugarcane growth stages during the agricultural season on sugarcane fields are presented in Fig. 3.

Sugarcane crops exhibit a distinctive pattern in their backscattering coefficients. In particular, σ° increased significantly from the establishment stage (February) to the grand growth stage (June). At the establishment stage, sugarcane plants presented low σ°_{VH} and σ°_{VV} averages. In the tillering phase (when sugarcane produces several stalks), σ° gradually increased, and continued until the grand growth phase (when sugarcane begins to grow rapidly and some stalks begin to grow). σ° is primarily influenced by changes in SM and surface roughness during the early growth stages when FVC is still low (Baghdadi et al. 2009). During the grand growth and ripening stages, $\sigma^{\circ}$is gradually reduced and attenuated by the development of the sugarcane canopy vertical structure. This period is characterized by volume scattering (Yuan et al. 2019). The beginning and end points of attenuation in the fields can be considered key points in the σ° time-series. In July, this attenuation began and continued until harvest. At 43.5°, it appears more intense than at 37.8°, and at σ°_{VH}, it appears more intense than at σ°_{VV}. It can be concluded that the observed σ° behavior is similar to that reported in previous studies (den Besten et al. 2023; Molijn et al. 2019): there is a significant increase in the first half of the season and a relatively slow decrease after the maximum is surpassed. It has been observed that the maximum in σ°_{VH} and σ°_{VV} occurs earlier than the maximum in optical indices. The σ°_{VV} values are larger than the σ°_{VH} values, and the intensity of decrease after maximum varies.

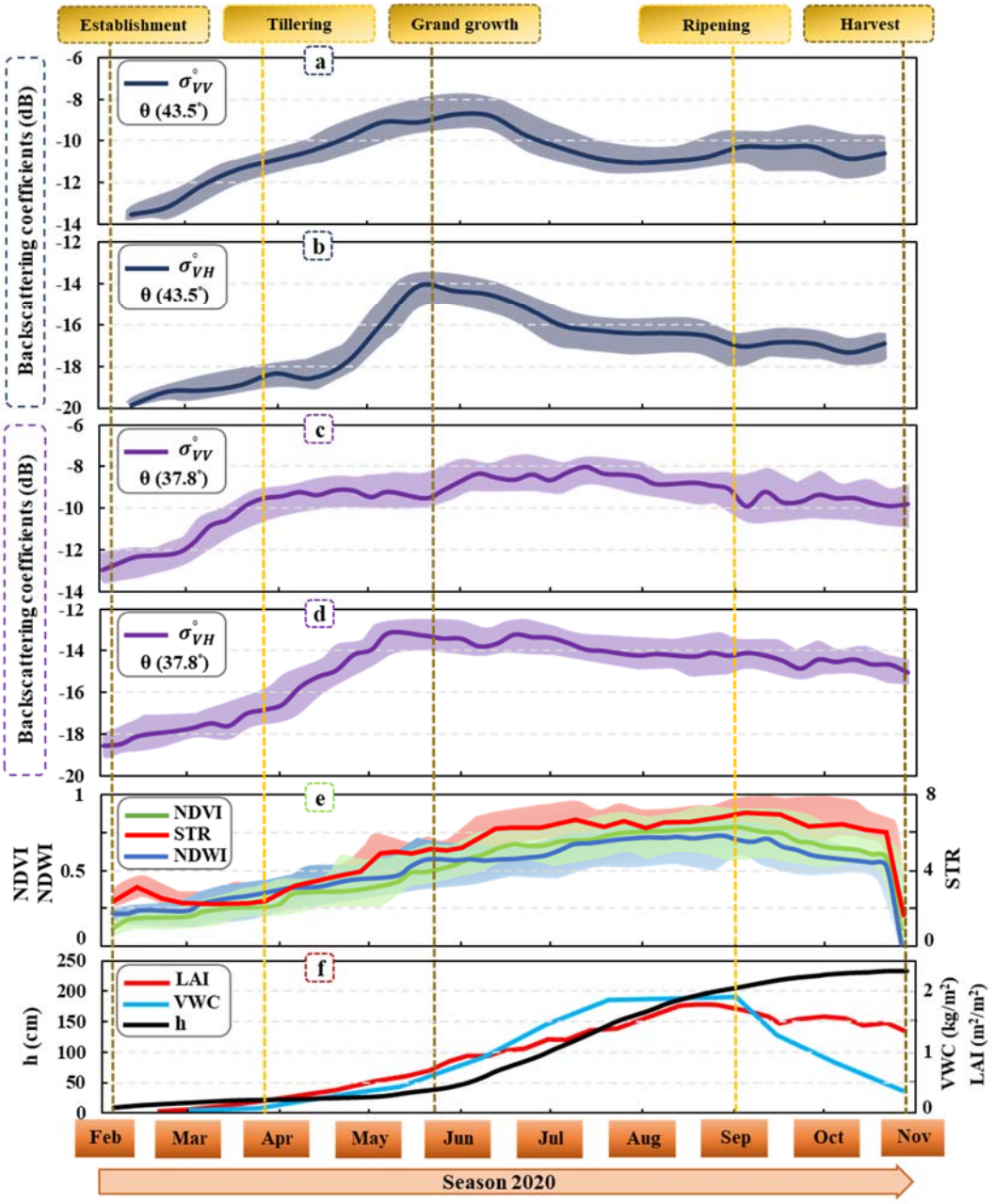

Figure 3. Time-series of σ°_{VV} and σ°_{VH} at (a and b) 43.5° and (c and d) 37.8°, (e) spectral indices and (f) vegetation parameters over sugarcane fields.

NDVI and NDWI showed similar dynamics (Fig. 3e), increasing immediately following the establishment phase to indicate early growth of sugarcane. At the middle of the grand growth stage (H_c > 150 cm), they reached a saturation plateau. They remained there until the ripening stage, when they showed a slight reduction, coincident with sugarcane ripening. As stated by Molijn et al. (2019), this reduction coincides with the decline in leaf biomass and the onset of senescence. LAI, NDVI and VWC seasonal trends are closely related. Nevertheless, the VWC decreases significantly after ripening in September, when nitrogen application and irrigation rates are reduced to slow down sugarcane growth, which results in more sugar accumulation on the stem (Fig. 3f). Further, the vertical distribution of VWC changes over the sugarcane growing season, which influences the observed σ°(den Besten et al. 2023). Over the whole season, VWC and LAI are not linearly related and their relationship depends on the canopy structure. In light of the above findings, it can be concluded that NDWI, NDVI and VWC have

more potential as vegetation descriptors for SM retrieval in sugarcane fields. The relationships between *in situ* SM and σ° are clearly scattered over the whole season. For a more detailed analysis, relationships were also examined in terms of LAI (m^2 m^{-2}). According to Table. 2, higher correlations found in this case (LAI < 1.1) are significant for all σ°. Due to the sugarcane canopy, the soil contribution to σ° is attenuated when sugarcane is grown (H_c > 90 cm and LAI > 1.1). Overall, σ°_{VV} is more closely correlated with SM than σ°_{VH}. The correlation between σ° and SM is higher at 37.8° than at 43.5°, since soil contributes more at a lower incidence angle.

Table 2. *R* values between *in situ* SM and σ° values in sugarcane and wheat fields.

	Sugarcane				**Wheat**			
	$\boldsymbol{\theta}$	LAI < 1.1	LAI > 1.1	Whole season	$\boldsymbol{\theta}$	LAI < 1.5	LAI > 1.5	Whole season
SM and σ°_{VV}	37.8°	0.72	0.18	0.36	35.2°	0.76	0.27	0.41
SM and σ°_{VH}		0.61	0.11	0.30		0.81	0.31	0.42
SM and σ°_{VV}	43.5°	0.63	0.09	0.29	45.6°	0.79	0.05	0.34
SM and σ°_{VH}		0.55	0.06	0.11		0.64	0.04	0.10

The time-series of S-1 backscattering coefficients (VV and VH) at 45.6° (ascending orbit) and 35.2° (descending orbit) incidence angles, NDVI, NDWI and STR from S-2 and *in situ* measurements at different wheat growth stages during two agricultural seasons on F1 (F2) are presented in Fig. 4 (Fig. S1). During each season, the schedule of stages is different. There is a distinctive pattern in the backscattering coefficients representing the wheat canopy, with distinct scattering dynamics during different growth stages as well as a seasonal trend in backscattering coefficients. In particular, σ° increased significantly from the sowing stage (December) to the emergence stage (January). σ° is primarily influenced by rapid changes in SM during the early growth stages when FVC is still low (Harfenmeister et al. 2019). During the extension (stem elongation) stage, σ° is gradually reduced and attenuated by the development of the wheat canopy vertical structure, reaching its minimum value at the heading stage. In February, this attenuation began and continued until March. After that, σ° increased again from flowering to ripening, although this second increase is less clear in F1 at 35.2°. However, it is evident in F2. At 45.6°, it appears more intense than at 35.2°, and at σ°_{VH}, it appears more intense than at σ°_{VV}. Several studies showed that a wet layer above the wheat canopy contributes to a second increase at the heading stage, especially when θ is above 40° (Mattia et al. 2003; Weiß et al. 2021). Furthermore, as stated in Balenzano et al. (2010), volume diffusion in the head layer triggers depolarization at the heading stage, resulting in a greater increase in σ°_{VH}. With the soil and wheat crops drying out during the ripening process, the final decrease lasted until harvest in June. It can be concluded that the observed σ° behavior is similar to that reported in previous studies (Palmisano et al. 2020; Villarroya-Carpio et al. 2022): the σ°_{VV} values are larger than the σ°_{VH} values, and the σ° dynamics vary with growth stage.

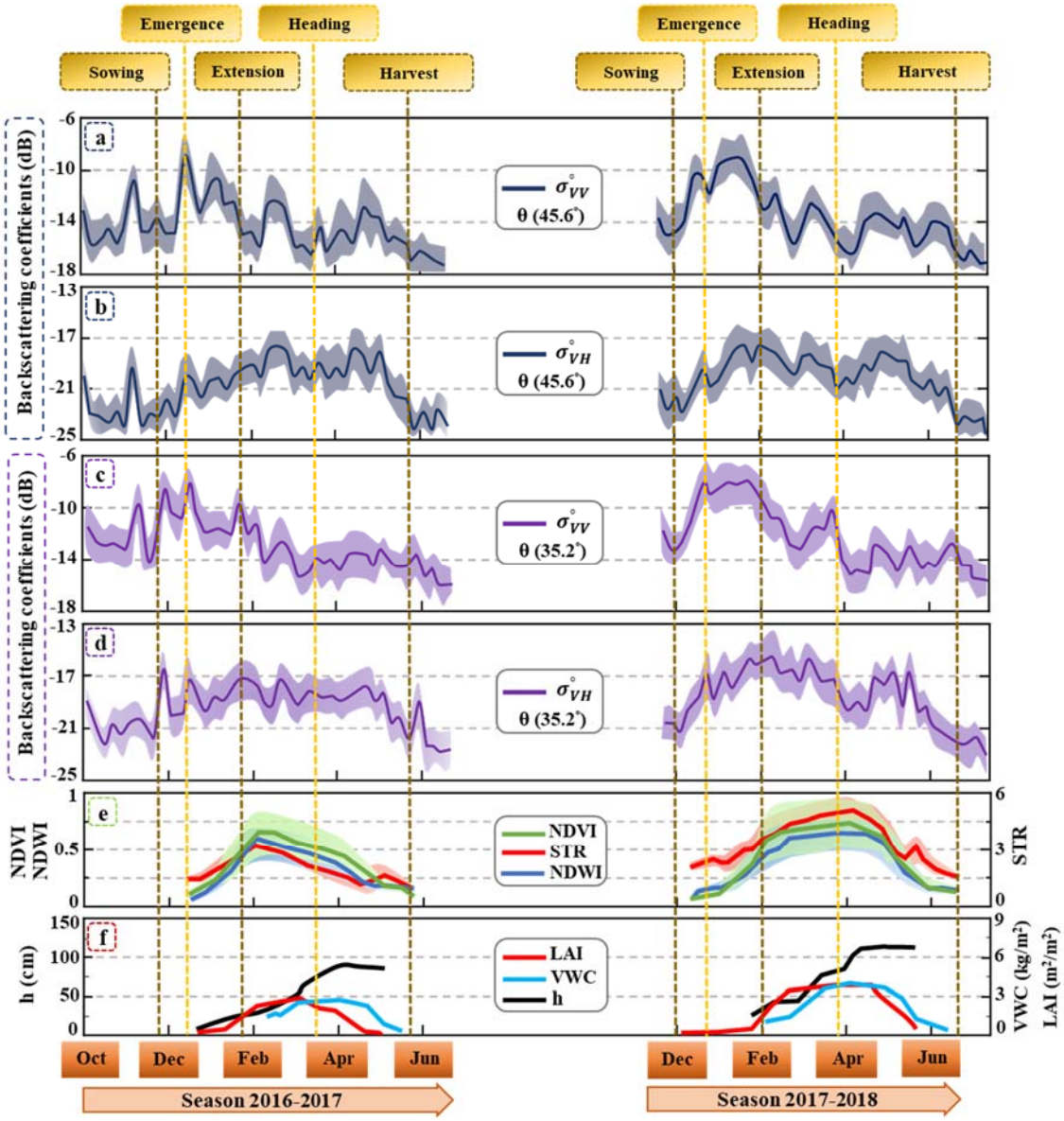

Figure 4. Time-series of σ°_{VV} and σ°_{VH} at (a and b) 45.6° and (c and d) 35.2°, (e) spectral indices and (f) vegetation parameters over F1 during two agricultural seasons.

For wheat fields, despite the fact that NDVI is largely dependent on LAI, VWC and LAI are not linearly related and their relationship depends on canopy structure. NDVI and NDWI showed similar dynamics (Figs. 4e and S1e), increasing immediately following emergence. After reaching a saturation plateau, they remained there until the ripening stage (Lawrence et al. 2014). A lack of S-2 time-series imagery caused by cloudy weather prevented the observation of this plateau in Season 2016-2017. The seasonal trend of both LAI and NDVI is closely related. A similar trend can be observed in VWC. However, maximum values of VWC are reached in the early days of April approximately 50 days after the maximum values for LAI and NDVI. The VWC also decreases significantly after heading in late April when stems and leaves have dried. In light of the above findings, it can be concluded that NDVI, LAI and VWC have more potential as vegetation descriptors for SM retrieval.

According to Table. 2, Observations indicate that larger correlations are seen between the σ° and the *in situ* SM values when the wheat canopy does not completely cover the underlying

soil. The correlations found in this case (LAI < 1.5) are significant for all σ°. At 35.2°, σ°_{VV} and σ°_{VH} exhibit somewhat similar relationships in wheat fields, but substantial differences favorable to σ°_{VV} are observed at 45.6°, as there is an increase in vegetation contribution with increasing incidence angles. In line with previous studies (Ayari et al. 2021; Bousbih et al. 2017): σ° sensitivity to SM is greater at low incidence angles and with VV polarization.

4.2. SAR and optical models

4.2.1. SAR models

A variety of vegetation descriptors (optical-derived or SAR-derived) were used to calibrate the WCM model, resulting in differences between the models. Several vegetation descriptors were evaluated during WCM calibration, including NDVI, NDWI, RVI and VWC. Here, we discuss the calibration results of the WCM model based on NDWI (VWC) for sugarcane (wheat) fields. These models were selected due to their better overall performance over other models. The time-series of observed and retrieved σ° on sugarcane (wheat) fields at, as well as the contribution of σ°_{soil} and σ°_{veg} when using NDWI (VWC), are presented in Fig. 5 (Figs. S2 and S3).

There is a good fit between the relative changes in the σ° (higher σ°_{VV} than σ°_{VH} and lower σ° at 43.5° than σ° at 37.8° for both VV and VH), indicating that the model is properly calibrated. With the development of the canopy, the soil contribution to scattering mechanisms decreases progressively. As the first half of the season (from February to June) progressed, the retrieval continued to be satisfactory. However, a bias gradually increased up to 4 dB in the ripening stage. The RMSE for the ripening stage was 2.5 dB more than for the entire season in sugarcane fields for σ°_{VV} at 37.8°. It was found that σ° differences are related to small deviations in SM retrieval of 0.02 m^3m^{-3} for the early stages, as well as large variations of 0.1 m^3m^{-3} during sugarcane canopy development. The SM retrieval deviations, however, increase during the second half of the season (From the middle of the grand growth stage).

According to the general evaluation of various WCM models, the NDWI-based WCM performed reasonably well during the early stages of the sugarcane crop season before the attenuation period in the grand growth stage began. As a consequence, the period of maximum attenuation was occurred in ripening stage. However, in late of tillering and beginning of grand growth, the VWC-based model retrieves σ° more accurately than the NDWI-based model. When incidence angles are low and sugarcanes are young, soil contributes significantly to the observed σ°. In this case, the σ° primarily represents surface roughness and soil moisture. Nevertheless, soil effects are small for sugarcanes with a well-developed canopy (LAI and H_c, respectively, exceeding 1.05 m2m-2 and 100 cm, depending on polarization and incidence angle). According to Baghdadi et al. (2009), the σ° in the C-band becomes less sensitive to soil parameters and more sensitive to canopy parameters as the plant grows. Several limitations exist during the second half of the season in all models: in well-developed sugarcane canopies (H_c > 200 cm), the influence of soil is relatively small due to volume scattering. The σ° is most likely more associated with the size, number and direction of sugarcane leaves. Therefore, the observed σ° in the second half of the season is determined by vegetation biomass (Molijn et al. 2019). It is evident that the retrieved σ° increased than the observed σ° at the end of the season. Due to these reasons, none of the SAR models could retrieve SM at an acceptable level during the second half of sugarcane growing season.

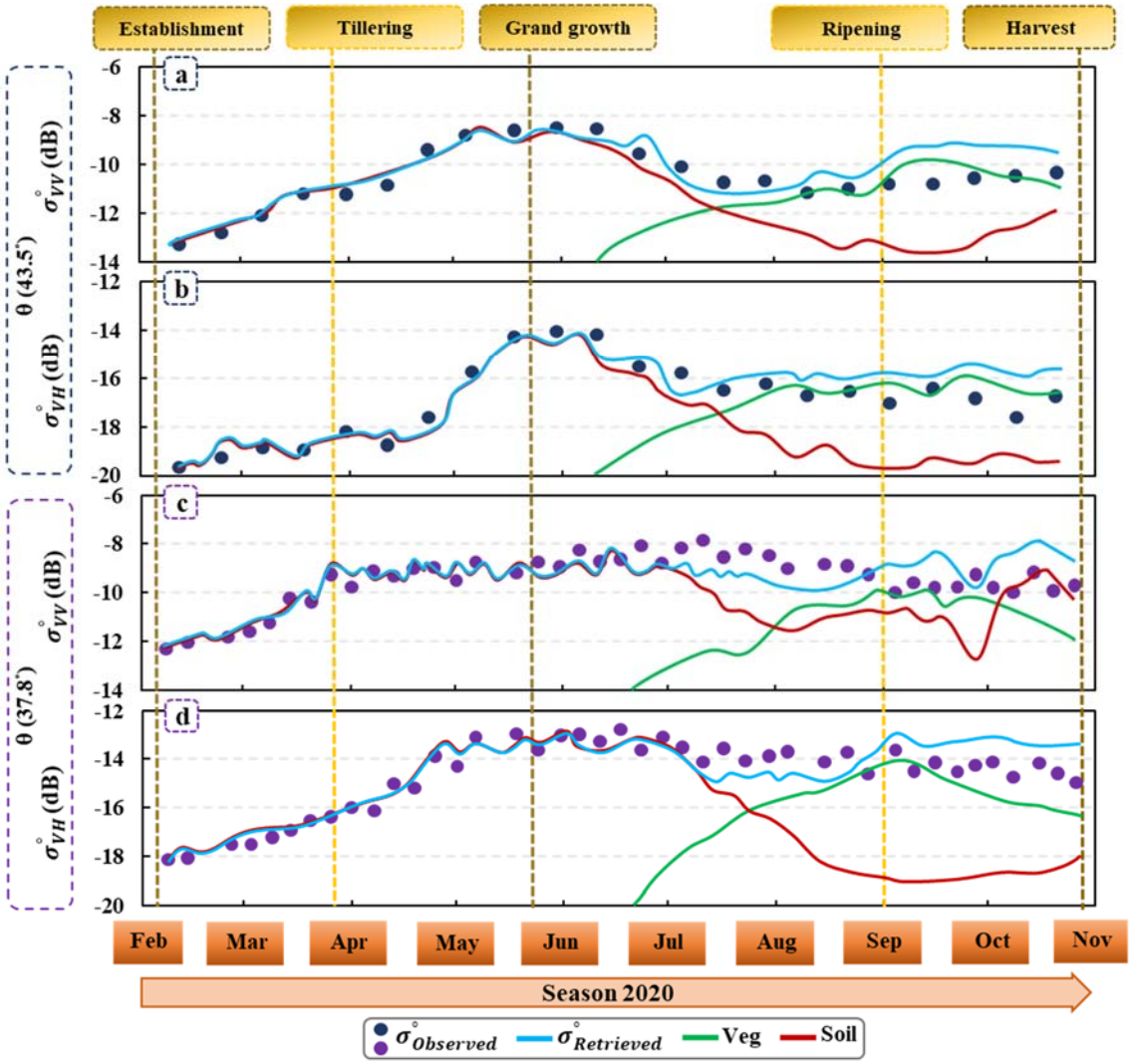

Figure 5. Time-series of observed and retrieved σ° based on WCM (vegetation descriptor: NDWI) over sugarcane fields at (a and b) 43.5° and (c and d) 37.8°.

In the case of wheat, Soil attenuation is higher in response to vertical stem extension for σ°_{VV} than for σ°_{VH}, consistent with Paloscia et al. (2014). As the first half of the season progressed, the retrieval continued to be satisfactory. However, a bias gradually increased up to 3 dB (3.5 dB) in F1 (F2) for σ°_{VV} at 35.2°. The RMSE for the heading stage was 1.5 dB (2.1 dB) more than for the entire season in F1 (F2) for σ°_{VV} at 35.2°. It was found that σ° differences are related to small deviations in SM retrieval of 0.017 m^3m^{-3} for the early stages, as well as large variations of 0.09 m^3m^{-3} during heading and canopy development. The SM retrieval deviations, however, increase during periods of significant vegetation growth (late in heading). According to the general evaluation of various WCM models, the NDVI-based WCM performed reasonably well during the early stages of the wheat crop season before the attenuation period in the extension stage began. As a consequence, the period of maximum attenuation was not accurately calculated since the sensitivity to further crop growth had decreased. However, after heading, the VWC-based model retrieves σ° more accurately than the NDVI-based model. Several limitations exist during the ripening process in the second half of the season in both models: (1) the observed decrease in σ° until the heading stage is poorly retrieved and (2) a rapid decline in vegetation indices results in a sudden decrease in σ° retrievals. It is evident

that the retrieved σ° decreased earlier than the observed σ° at the end of the season, particularly in σ°_{VH} (see Figs. S3b and S3d).

In comparison with other optical-derived descriptors, the NDVI-based (NDWI-based) WCM models showed greater differences between the observed and retrieved σ° values of sugarcane (wheat) fields, which means less accuracy. A WCM based on RVI (SAR-derived descriptor) produced relatively low accuracy at the maximum attenuation points, with the differences between the observed and retrieved σ° time-series increasing as the sugarcane (wheat) developed. Of the different SAR models, some models performed better at the early stages of crop growth while others performed better at later stages. When selecting just one SAR model, the WCM model based on NDWI (VWC) provided the most accurate retrieval of the σ° time-series in terms of overall RMSE compared to the other SAR models for sugarcane (wheat) fields. It was possible to distinguish clearly the attenuation in the retrieved backscattering coefficients in all fields after calibrating the WCM using any vegetation descriptor. The corresponding RMSEs of the different WCM models are presented in Fig. 9.

4.2.2. Optical models

For sugarcane (wheat) fields, STR-VI spaces were derived using vegetation indices (NDVI, SAVI and LAI) and STR, based on two parameterization approaches (linear and nonlinear), and evaluated. Here, we discuss the results of the OPTRAM models based on STR-NDVI space (Figs. 6 and S4). In the early stages of crop growth (establishment to tillering for sugarcane and sowing to emergence for wheat), the OPTRAM parameters are not applicable because the NDVI values are small and the STR-NDVI space is not sufficiently developed.

The OPTRAM model was parameterized using data from the integrated STR-NDVI space, acquired between February and October 2020 for sugarcane fields. During the tillering stage of sugarcane crops in late March, NDVI increased slightly as the growth of the crops increased. STR and NDVI both continued to increase progressively until the ripening stage was reached before September. In light of this behavior, the linear OPTRAM was able to estimate SM more accurately than the nonlinear OPTRAM at the grand growth stage until the ripening stage. At the ripening stage, STR peaked around the NDVI value of 0.78. The performance of nonlinear OPTRAM was superior to that of linear OPTRAM from the ripening stage until harvest. This is due to the possibility of more complex relationships occurring in the STR-NDVI space as the sugarcane canopy develops.

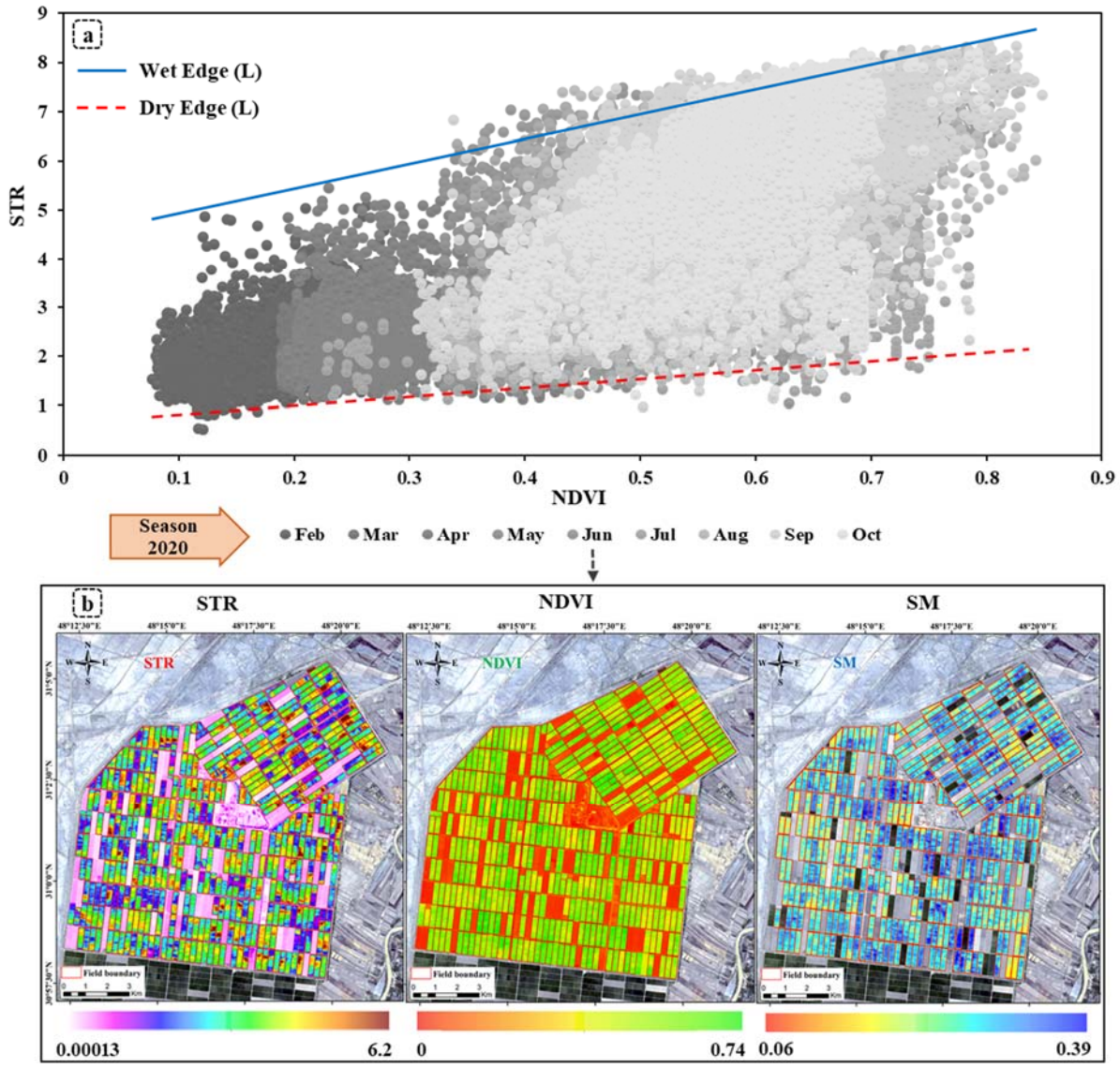

Figure 6. (a) Pixel distribution within the integrated STR-NDVI space for the 2020 season. (b) STR, NDVI and SM retrieval derived using OPTRAM over sugarcane fields (14 June 2020).

Since the STR-NDVI space was stable in 2017-2018 (Fig. S4a), the OPTRAM model was parameterized using data from the integrated STR-NDVI space, acquired between December 2017 and June 2018 for wheat fields. During the emergence stage of wheat crops in late December, NDVI increased slightly as the growth of the crops increased. STR and NDVI both continued to increase progressively until the heading stage was reached before April. After the heading stage, STR peaked around the NDVI value of 0.69 (0.88) in F1 (F2). However, in May, the peak moved to the NDVI value of 0.28 (0.47) in F1 (F2). This is because water above saturated SM has the potential to increase STR, but SM is limited to this saturation level (Sadeghi et al. 2017). Between March and June, pixels are arranged in a trapezoidal pattern on the scatterplots. The results are in line with the OPTRAM concept, providing more accurate estimation of SM from March to June. The performance of nonlinear OPTRAM was superior to that of linear OPTRAM from the heading stage until harvest.

The application of OPTRAM over the entire growing season was limited. The OPTRAM models in this research were able to achieve satisfactory performance, similar to the theoretical model, during the second half of the season. The models, however, had low accuracy at the

beginning of the season. As representative optical models, the OPTRAM models used in this research for SM estimation produced greater accuracy during the middle and late stages of the crop growth cycle. It should be noted that there are differences between the STR-SAVI and STR-NDVI spaces in estimating SM with OPTRAM. The estimates based on SAVI were slightly more accurate than those based on NDVI on some dates of the season.

4.3. SM retrieval based on DL-MME and comparison with individual models

As a means of demonstrating the effects of hyperparameter tuning on retrieval accuracy, various sets of hyperparameters were evaluated for each hyperparameter. One hyperparameter was changed at a time, while others remained unchanged. Here, we discuss the hyperparameter tuning of the DL-CNN algorithm in case of wheat fields. According to the R and RMSE values for the validation step obtained with different learning rates and batch sizes (Figs. 7a and 7b), the optimal learning rate (α) and batch size (ω) are 0.1 and 50, respectively. As shown in Fig. 7c, in terms of the number of convolutional layers (ι), the optimal number is 5. In response to an increase in ι, R increases initially, and decreases when ι increases beyond 5. The RMSE, however, decreases initially and then increases. It is clear from the hyperparameter tuning step that the DL-CNN algorithm learns more effectively when the learning rate is 0.1, the batch size is 50, and the number of convolutional layers is 5. This is because the model can better capture learning patterns with these hyperparameters to increase retrieval accuracy. To achieve a normal distribution of random weights, the kernel initializer was set to 'normal'. From the training process with the hyperparameters discussed above, the trained DL-CNN was obtained.

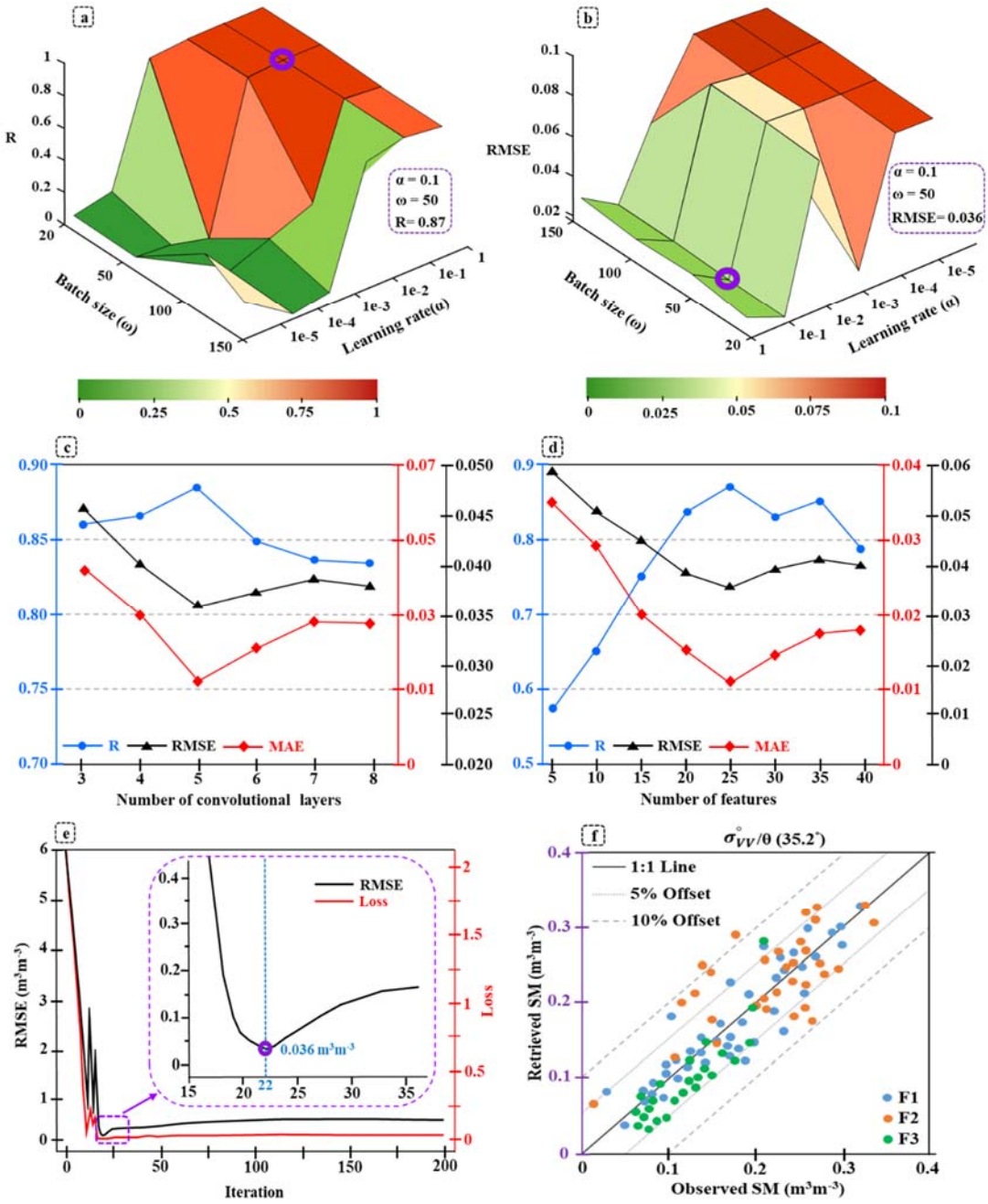

Figure 7. Impacts of three hyperparameters and number of features on SM retrieval accuracy over wheat fields. (a) *R* values for the validation step obtained from various learning rates and batch sizes; (b) RMSE values for the validation step obtained from various learning rates and batch sizes; (c) RMSE, *R* and MAE values for the validation step obtained from various numbers of convolutional layers; (d) RMSE, *R* and MAE values for the validation step obtained from various numbers of features. (e) Relations between SM retrieval accuracy and the number of iterations in the validation step in DL-CNN. (f) Scatterplot of the retrieved and observed SM (obtained from *in situ* measurements) in the test step for σ°_{VV} at 35.2°.

As shown in Fig. 7d, DL-CNN retrieval accuracy in the validation step increased significantly as the number of features increased (20), followed by a gradual increase to 25 features. The *R* value between observed and retrieved SM increased to a maximum value of 0.87 as the number of features increased to 25, and the RMSE reached a minimum value of 0.036 m^3 m^{-3}. Following that, as the number of features increased, the RSME gradually increased. This

indicates that with an increase in the number of features, the DL-CNN algorithm was able to more accurately identify the relationship between the observed and retrieved SM. The highest accuracy was achieved with 25 features, indicating that this is the optimal number of features to use for this model in the present case. Therefore, it is not necessary to use more features than 25 to improve SM retrieval. As shown in Fig. 7e, the DL-CNN retrieval accuracy changes sharply as the number of iterations increases. The accuracy tends to remain constant after a certain number (about 80). The lowest RMSE (0.036 m^3m^{-3}) between the observed and retrieved SM was achieved after 22 iterations. However, accuracy decreases gradually as iteration times increases. Therefore, iteration number will have a significant effect on the SM retrieval results after the DL-CNN has been constructed. Therefore, it is recommended to adjust the number of iterations carefully according to the minimum RMSE value to retrieve SM more accurately. According to the SM scatterplot of wheat fields (Fig. 7f), most points fall within the error range of 5%. During the 2017-2018 season, certain growth conditions in F2 (wild thistles and wind effects), which were discussed by Ouaadi et al. (2021), adversely affected the models' performance, as evidenced by the poor results achieved on F2.

The importance score of a variety of effective features over the whole season was assessed to increase SM retrieval accuracy (Fig. 8). For feature importance evaluation, all training samples were used. The importance scores of Group A features (SAR and optical models) were significantly higher than those of other features (Group B and C). Over the whole wheat crop season, WCM-AIEM$_{VWC}$ (0.74), WCM-Oh$_{VWC}$ (0.71), and WCM-AIEM$_{NDVI}$ (0.69) received the highest importance scores for SM retrieval based on DL-MME. DVI and CCC scored 0.13 and 0.16, respectively, in terms of lowest importance. Overall, NL-OPTRAM$_{NDVI}$ (0.63) produced the most significant contribution among the optical models. Evaluation results indicate that SAR and biomass features contribute more to SM retrieval than optical indices in the case of wheat. Among the SAR features, biomass features and optical indices, PR (0.42), CWC (0.34) and NDVI (0.29) were the most significant, respectively (Fig. 8b).

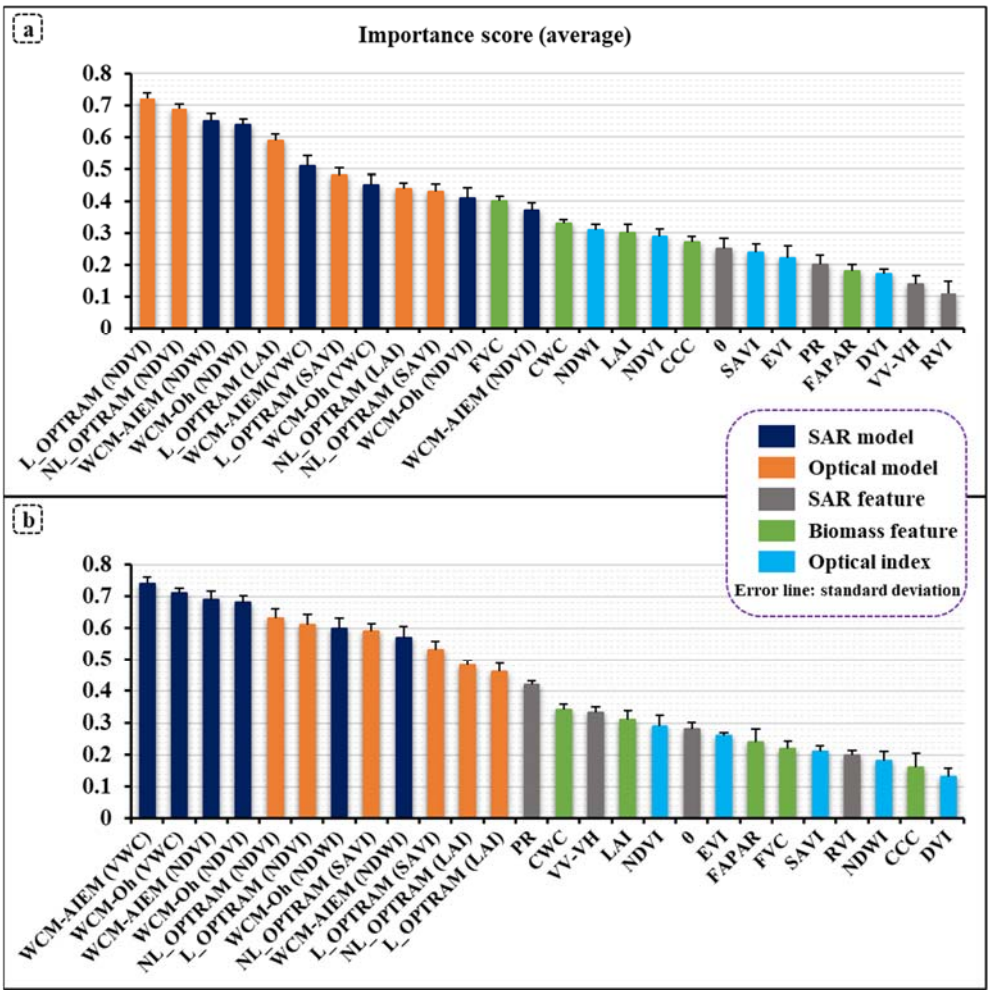

Figure 8. Average of importance score of each input feature over the whole season for sugarcane fields (a) and wheat fields (b).

However, when it comes to sugarcane, L-OPTRAM$_{NDVI}$ (0.72), NL-OPTRAM$_{NDVI}$ (0.69), and WCM-AIEM$_{NDWI}$ (0.65) received the highest importance scores for SM retrieval based on DL-MME. RVI and VV-VH scored 0.11 and 0.14, respectively, in terms of lowest importance. Evaluation results indicate that biomass features and optical indices contribute more to SM retrieval than SAR features in the case of sugarcane. Among the SAR features, biomass features and optical indices, θ (0.25), FVC (0.4) and NDWI (0.31) were the most significant, respectively (Fig. 8a).

Different configurations (combinations of features) were evaluated in terms of retrieval accuracy. It was found that the DL-MME accuracy in the case of wheat (sugarcane) was higher with a RMSE of 0.036 (0.074) m^3m^{-3} and a R of 0.87 (0.71) when features from both S-1 and S-2 data were included alongside SAR and optical models (i.e., Configuration G), compared to Configurations E and F when only optical (Group B) or SAR (Group C) features were combined with Group A. All three groups were utilized in the DL-MME method to achieve the highest overall accuracy. It is noteworthy that SAR features from Group C may be more effective in SM retrieval for wheat and optical features from Group B may be more effective in SM retrieval for sugarcane.

As a further step, the retrieval accuracies for each crop under different models were compared to assess the contribution of each model at different crop growth stages. The SAR model (e.g., WCM-AIEM$_{NDVI}$ or WCM-AIEM$_{VWC}$) retrieved SM of wheat fields relatively well at the

beginning of the season, with a RSME of 0.032 m^3m^{-3} and the middle season with a RSME of 0.05 m^3m^{-3}. However, it had difficulties retrieving SM content during the second half of the growing season, especially after the heading stage. In contrast, when only using optical models, time-series SM retrieval accuracy was high in the second half of the growth season, with a RSME ranging from 0.05 to 0.043 m^3m^{-3}.

The DL-MME produced a lower RMSE and higher *R* values than the individual models at different dates of the growth season. Wheat (sugarcane) growth during the season stages generally affected DL-MME performance, but the effect was slightly more significant after heading (grand growth) stage (see Fig. 10 in section 5). In wheat crop season, during both the sowing and emergence stages, the lowest RMSEs of 0.031 and 0.033 m^3m^{-3} were observed, whereas after the heading stage in late April the highest RMSE of 0.045 m^3m^{-3} was observed. Also, for sugarcane crop, during the establishment stage the lowest RMSE of 0.037 m^3m^{-3} was observed, whereas after the ripening stage in September the highest RMSE of 0.087 m^3m^{-3} was observed. A major contribution of SAR and optical models can be observed in the increases in the retrieval accuracy of the time-series SM based on DL-MME. The average RMSE values of some models for fields over the whole season are presented in Fig. 9. More detailed and complementary results about the accuracy assessment of SM retrieval based on various models are provided in Table S1.

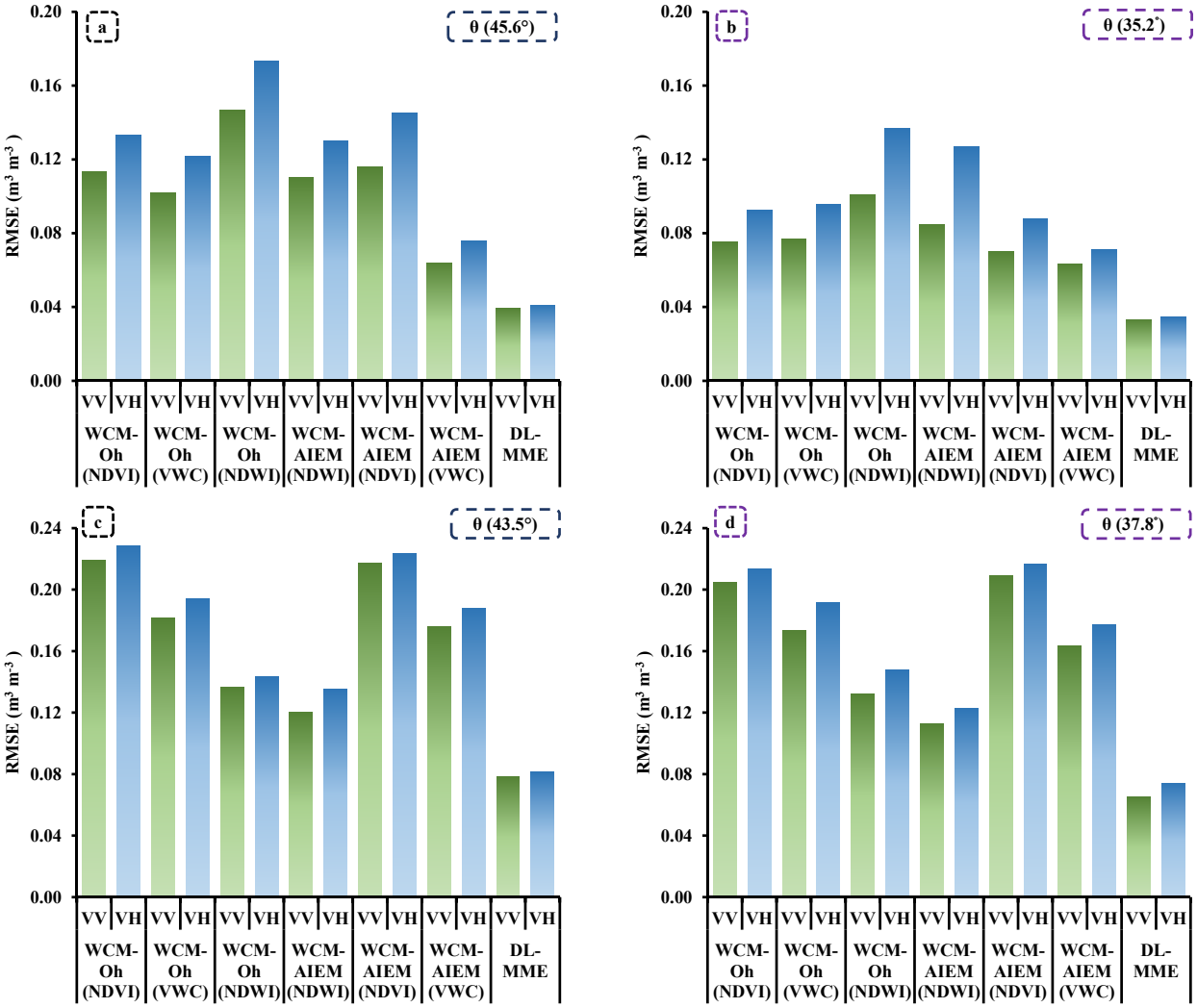

Figure 9. The average RMSE of different models for wheat fields at (a) 45.6° and (b) 35.2°, and for sugarcane fields at (c) 43.5° and (d) 37.8°.

The lowest average RMSE values in wheat (sugarcane) fields over the whole season were achieved by DL-MME for σ°_{VV} at 35.2° (37.8°) which was 0.033 (0.065 m^3m^{-3}). Based on the results, DL-MME it can be seen that retrieves SM more accurately than the individual models. DL-MME achieved optimal results across all three metrics (RSME, *R* and MAE). Additionally, it demonstrated high consistency across different incidence angles for the whole season. This highlights the potential of DL-MME as a powerful deep learning-based framework for SM retrieval from multiple models and various sources of remote sensing data.

5. Discussion

A DL-MME method does not require prior model selection. Moreover, the models (input parameters) in our framework do not require precise calibration during the crop growth season. It is evident that retrieval accuracy can be increased considerably if the models are calibrated perfectly. With regard to the WCM model as an example of a SAR model, our findings regarding the effect of different vegetation descriptors on the calibration process were consistent with those revealed in previous studies. It is generally considered that WCM is a simple and straightforward model to implement, although its calibration and retrieval capabilities may vary from site to site and be unstable over time and space (Bouchat et al. 2022). Several studies have reported similar results for NDVI-based and NDWI-based WCM. Several studies indicated that NDWI-based WCM results in better SM retrieval than NDVI-based WCM (Bao et al. 2018; Wang et al. 2020), because the SWIR band has a higher sensitivity to VWC, while the NDVI has a relatively low sensitivity to vegetation growth after a value of 0.8 (Baghdadi et al. 2017). Opposed to this, Zhang et al. (2021) reported limited results using an NDWI-based WCM, attributed to VWC saturation. Several studies found reliable results when using LAI-based WCM (El Hajj et al. 2016; Weiß et al. 2020). One of the key issues in the WCM model is access to cloud-free optical images during the crop growing season. WCM may benefit from SAR-derived vegetation descriptors, such as PR and RVI, since these descriptors provide calibration without optical images. WCM models based on SAR-derived descriptors (RVI, PR and VV-VH), in our study did not perform well during the crop growing season, although Wang et al. (2021b) reported better results using VH polarization as a vegetation descriptor for other crop types. Nevertheless, few attempts at this exist, producing unsatisfactory results. Optical models such as OPTRAM are also subject to similar discussions, so that some studies with different parameterization schemes have achieved different results (Ambrosone et al. 2020; Ma et al. 2022). Although the OPTRAM model performed well for SM estimation, it had several practical limitations. First, uncertainty exists in the definition of the OPTRAM parameters. It is possible that the SM estimates will change if the intercepts and slopes of the wet and dry edges change. Additionally, in some cases the underlying surface limits the OPTRAM model's performance for SM estimation. This is because the OPTRAM model is highly sensitive to oversaturated pixels (Babaeian et al. 2018; Sadeghi et al. 2017). Furthermore, as observed in the first season of our research, clouds limit the availability of optical data. It can be concluded that to achieve high accuracy, the single-model must undergo perfect calibration or parameterization during the crop growth season, which is almost impossible. For example, the calibration of WCM model can be challenging when different crops are involved or when *in situ* measurements are not available.

It should be noted that each SM value represents potentially a number of observable backscattering coefficients (points in STR-NDVI space), whose range varies significantly, resulting in some uncertainty in SM value retrieval. This implies that SM retrieval can be

viewed as a high-dimensional problem. As part of the single-model retrieval method, SM values are assigned based on the relevant backscattering coefficients (or STR-NDVI space) information after calibration (or parameterization). Nevertheless, when retrieving time-series SM, the models applied might need some flexibility in terms of their method framework in order to account for any potential scattering mechanisms and their weighting as a function of growth stage. As a result, retrieval error can be reduced through step-by-step optimal computation using the DL-MME method, thereby bringing the accuracy of SM retrieval to its highest level. It was shown in our study areas that four (five) models contribute significantly to retrieving the time-series SM over sugarcane (wheat) fields during the agricultural season with high accuracy (Fig. 10). According to our findings, despite the fact that the importance of models utilizing different data sources may differ, all models contributed to improving retrieval performance.

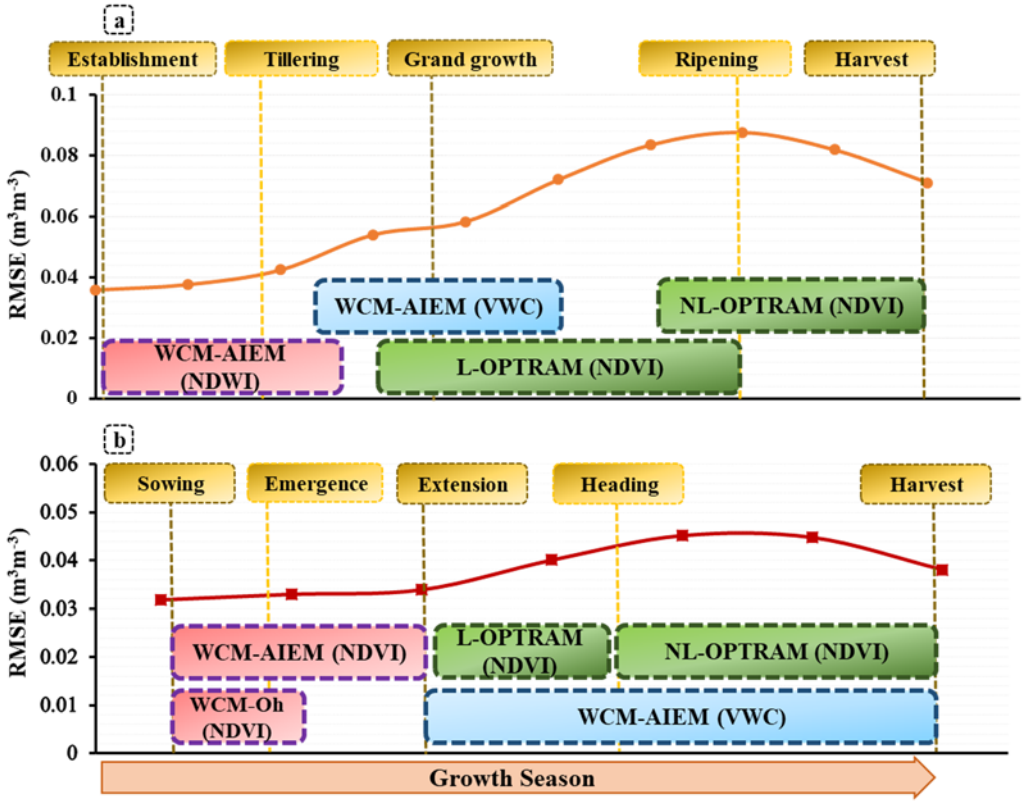

Figure 10. The optimal combination based on DL-MME to retrieve time-series SM during the sugarcane (a) and wheat (b) growth season.

Studies have demonstrated that optical and active microwave time series can provide valuable information about phenology stages, such as NDVI, LAI, VWC, and biomass, in agricultural fields since SM retrieval depends heavily on reliable canopy information (Ouaadi et al. 2020; Pipia et al. 2019). Additionally, Wang et al. (2023) and Zhang et al. (2022) showed that machine learning techniques can effectively ingest information extracted from different sources and enhance SM retrieval. In addition to being an effective machine learning methodology, deep learning has also demonstrated efficiency in establishing more predictive relationships between SM and various covariates. According to El Hajj et al. (2017), neural networks are suitable for solving the SM retrieval problem because they possess capabilities such as function approximation and optimization computation. The DL-MME framework was able to improve complex calculations needed for SM retrieval during the crop growth season by using information from time-series interpretation, multiple models and the capabilities of

DL. In this research, the accuracy assessment indicated improved SM retrieval in comparison with those obtained by Ouaadi et al. (2020) in the same study area. In their study, Ouaadi et al. used a relationship found between AGB and VV interferometric coherence as a vegetation descriptor and achieved a RMSE of 0.05 m^3m^{-3}. In this comparison, it was evident that DL is an effective inversion method and that optical models are an effective component of our framework as well.

One of the strengths of the present research is that models (features) can be pre-selected by a moderator. An ensemble approach can be hampered if poor models are predominant. Additionally, increasing model numbers does not seem to offer much benefit (Murphy 2012). Currently available multi-model ensembles are computationally expensive, and it is possible to bias the retrieved parameters in favor of a particular model. In principle, it is possible to combine the most powerful models by leveraging their unique strengths, but the process requires reliable and independent characterization of each model (Stumpf 2020). This research demonstrated that the proposed DL-MME framework is reliable when the ensembles are constructed correctly. It was found that DL-MME performance is negatively impacted by the poor performance of some models. Thus, models with low weights in multi-model combinations or poorly performing models were excluded from DL-MME by the moderator.

Generally, the DL-MME method offers an integrated framework for retrieving SM systematically in complex agricultural fields. Certain conditions must be met for DL to be considered an optimal method rather than a black box (Wang et al. 2021a). Firstly, the input parameters must be capable of determining the output parameters as well as establishing a causal relationship between them, which is the necessary condition. Then, the input parameters are theoretically capable of constructing sufficient equations and the output results can be derived from those equations, which is the sufficient condition. The DL-MME method is capable of enriching the theoretical context of SM retrieval and making it useful for practical purposes.

5.1. Challenges and future research

This research proposed the DL-MME to solve practical problems of SM retrieval via a multi-model ensemble within the DL framework. Although significant progress was achieved with this method, major challenges remain that should be addressed in future research. A first consideration is the influence of models and features. Ensemble models based on DL-CNN are generally more stable than single models, but the computational cost is higher. It is generally more time-consuming to apply the DL-MME method than individual methods. Consequently, it is necessary to further investigate and analyze the complexity of DL-MME, including the number of models and the time required for calculations, to determine whether this level of complexity is acceptable.

In the proposed framework, a second challenge is selecting the appropriate DL algorithm. Several remote sensing retrieval tasks have shown that CNNs play an important role, including retrieval of SM (Wang et al. 2018). However, CNNs have some drawbacks, including the need for large quantities of training data and high computational costs (Yuan et al. 2020). It is still very difficult to obtain adequate quantities or quality of *in situ* (labeled) data for some remotely sensed SM models employed in agricultural fields (e.g., surface roughness). As a result, it is necessary to further investigate the performance of other DL algorithms, such as semi-supervised learning, self-supervised learning and transfer learning. It was been shown that such strategies are capable of alleviating some of the problems associated with inadequate labeled data (Ge et al. 2022).

Another challenge for DL-MME is to incorporate uncertainty estimation into its architecture. It is imperative that there are many sources of uncertainty in the SM retrieval problem. Input data (e.g., noise effects), model calibration (parameterization), and the DL algorithm itself are sources of uncertainty. This requires the estimation of the method output uncertainty (Raissi et al. 2019). Most current DL algorithms do not provide uncertainty measures for predictions (Dechesne et al. 2021). To evaluate uncertainty in DL, various uncertainty quantification techniques can be used (Abdar et al. 2021). A follow-up study on DL-MME would be beneficial to explore how uncertainty is represented and assessed. In the future, further research should be conducted to test the effectiveness of DL-MME in agricultural areas with different climate conditions and for other crop types (such as maize, soybean, etc.) with more complex patterns and different scattering mechanisms.

6. Conclusions

A new DL-MME method for SM retrieval based on multi-model ensembles and DL was proposed. We investigated comprehensively the time-series interpretation of backscattering coefficients and vegetation descriptors, the relationships between parameters, advantages and disadvantages of SAR and optical models and the combination of models to obtain optimal high retrieval accuracy depending on crop (wheat/sugarcane) growth stage during the agricultural season. A multiple model ensemble approach using a deep learning framework is recommended to solve the SM retrieval problem, which relies on the connections between features. Results indicated that DL-MME has much higher retrieval accuracy than individual semi-empirical SAR and optical models. As a result of validation using *in situ* measurements, the minimum MAE achieved by the optimal combination is less than 0.01 m^3m^{-3} (0.02 m^3m^{-3}) during the wheat (sugarcane) growth season. The *in situ* validation showed that the minimum RMSE obtained from the optimal combination is approximately 0.036 m^3m^{-3} (R = 0.87) for wheat fields and 0.074 m^3m^{-3} (R = 0.71) for sugarcane fields. With more models at different growth stages, the retrieval accuracy of the SM can increase, while with SAR features, more accurate results are obtained under cloudy conditions. However, when optical data are not available and WCM models run with SAR descriptors, retrieval accuracy is not significantly improved. In summary, our results showed that there is potential to generate accurate time-series SM at a fine spatial resolution (20 m) within agricultural fields, which is important for agricultural applications. The DL-MME framework is model and sensor independent. Moreover, the DL-MME framework is easily generalizable to other models (i.e. radiative transfer models (RTM) or TIR-based models) and satellite sensor imagery (i.e. Landsat 8/9, GF-1/3 and L-band missions such as ALOS-2 or SAOCOM). Perhaps even more importantly, deep learning-based frameworks can be utilized as a viable and alternative method for retrieving full gap-free time-series SM from agricultural fields in the absence suitably fitted physical models.

Acknowledgements

The authors would like to acknowledge the Sugarcane & By Products Development Company of Khuzestan for providing ground measurement data from sugarcane fields. Also, the authors thank Ouaadi et al., for sharing freely accessible the Wheat fields database (https://doi.org/10.23708/8D6WQC) used in our research. The authors thank the RSASE Editorial team and the anonymous reviewers for their constructively critical comments and suggestions which improved an earlier version of this research.

References

Abdar, M., Pourpanah, F., Hussain, S., Rezazadegan, D., Liu, L., Ghavamzadeh, M., Fieguth, P., Cao, X., Khosravi, A., & Acharya, U.R. (2021). A review of uncertainty quantification in deep learning: Techniques, applications and challenges. *Information Fusion, 76*, 243-297

Alzubaidi, L., Zhang, J., Humaidi, A.J., Al-Dujaili, A., Duan, Y., Al-Shamma, O., Santamaría, J., Fadhel, M.A., Al-Amidie, M., & Farhan, L. (2021). Review of deep learning: Concepts, CNN architectures, challenges, applications, future directions. *Journal of big Data, 8*, 1-74

Ambrosone, M., Matese, A., Di Gennaro, S.F., Gioli, B., Tudoroiu, M., Genesio, L., Miglietta, F., Baronti, S., Maienza, A., & Ungaro, F. (2020). Retrieving soil moisture in rainfed and irrigated fields using Sentinel-2 observations and a modified OPTRAM approach. *International Journal of Applied Earth Observation and Geoinformation, 89*, 102113

Attema, E., & Ulaby, F.T. (1978). Vegetation modeled as a water cloud. *Radio science, 13*, 357-364

Autret, M., Bernard, R., & Vidal-Madjar, D. (1989). Theoretical study of the sensitivity of the microwave backscattering coefficient to the soil surface parameters. *Remote Sensing, 10*, 171-179

Ayari, E., Kassouk, Z., Lili-Chabaane, Z., Baghdadi, N., Bousbih, S., & Zribi, M. (2021). Cereal crops soil parameters retrieval using L-band ALOS-2 and C-band sentinel-1 sensors. *Remote Sensing, 13*, 1393

Ayari, E., Kassouk, Z., Lili-Chabaane, Z., Baghdadi, N., & Zribi, M. (2022). Potential of the Modified Water Cloud Model to Estimate Soil Moisture in Drip-Irrigated Pepper Fields Using ALOS-2 and Sentinel-1 Data. In, *IGARSS 2022-2022 IEEE International Geoscience and Remote Sensing Symposium* (pp. 5700-5703): IEEE

Babaeian, E., Sadeghi, M., Franz, T.E., Jones, S., & Tuller, M. (2018). Mapping soil moisture with the OPtical TRApezoid Model (OPTRAM) based on long-term MODIS observations. *Remote sensing of environment, 211*, 425-440

Baghdadi, N., Boyer, N., Todoroff, P., El Hajj, M., & Bégué, A. (2009). Potential of SAR sensors TerraSAR-X, ASAR/ENVISAT and PALSAR/ALOS for monitoring sugarcane crops on Reunion Island. *Remote sensing of environment, 113*, 1724-1738

Baghdadi, N., El Hajj, M., Zribi, M., & Bousbih, S. (2017). Calibration of the water cloud model at C-band for winter crop fields and grasslands. *Remote Sensing, 9*, 969

Baghdadi, N., Holah, N., & Zribi, M. (2006). Calibration of the integral equation model for SAR data in C-band and HH and VV polarizations. *International Journal of Remote Sensing, 27*, 805-816

Bai, X., He, B., Li, X., Zeng, J., Wang, X., Wang, Z., Zeng, Y., & Su, Z. (2017). First assessment of Sentinel-1A data for surface soil moisture estimations using a coupled water cloud model and advanced integral equation model over the Tibetan Plateau. *Remote Sensing, 9*, 714

Balenzano, A., Mattia, F., Satalino, G., & Davidson, M.W. (2010). Dense temporal series of C-and L-band SAR data for soil moisture retrieval over agricultural crops. *IEEE Journal Of Selected Topics In Applied Earth Observations And Remote Sensing, 4*, 439-450

Bao, Y., Lin, L., Wu, S., Deng, K.A.K., & Petropoulos, G.P. (2018). Surface soil moisture retrievals over partially vegetated areas from the synergy of Sentinel-1 and Landsat 8 data using a modified water-cloud model. *International Journal of Applied Earth Observation and Geoinformation, 72*, 76-85

Barrett, B.W., Dwyer, E., & Whelan, P. (2009). Soil moisture retrieval from active spaceborne microwave observations: An evaluation of current techniques. *Remote Sensing, 1*, 210-242

Ben Abbes, A., & Jarray, N. (2022). Unsupervised self-training method based on deep learning for soil moisture estimation using synergy of sentinel-1 and sentinel-2 images. *International Journal of Image and Data Fusion*, 1-14

Bouchat, J., Tronquo, E., Orban, A., Neyt, X., Verhoest, N.E., & Defourny, P. (2022). Green Area Index and Soil Moisture Retrieval in Maize Fields Using Multi-Polarized C-and L-Band SAR Data and the Water Cloud Model. *Remote Sensing, 14*, 2496

Bousbih, S., Zribi, M., El Hajj, M., Baghdadi, N., Lili-Chabaane, Z., Gao, Q., & Fanise, P. (2018). Soil moisture and irrigation mapping in A semi-arid region, based on the synergetic use of Sentinel-1 and Sentinel-2 data. *Remote Sensing, 10*, 1953

Bousbih, S., Zribi, M., Lili-Chabaane, Z., Baghdadi, N., El Hajj, M., Gao, Q., & Mougenot, B. (2017). Potential of Sentinel-1 radar data for the assessment of soil and cereal cover parameters. *Sensors, 17*, 2617

Brogioni, M., Pettinato, S., Macelloni, G., Paloscia, S., Pampaloni, P., Pierdicca, N., & Ticconi, F. (2010). Sensitivity of bistatic scattering to soil moisture and surface roughness of bare soils. *International Journal of Remote Sensing, 31*, 4227-4255

Champagne, C., White, J., Berg, A., Belair, S., & Carrera, M. (2019). Impact of soil moisture data characteristics on the sensitivity to crop yields under drought and excess moisture conditions. *Remote Sensing, 11*, 372

Chen, K.-S., Wu, T.-D., Tsang, L., Li, Q., Shi, J., & Fung, A.K. (2003). Emission of rough surfaces calculated by the integral equation method with comparison to three-dimensional moment method simulations. *IEEE Transactions on Geoscience and Remote Sensing, 41*, 90-101

Chen, M., Zhang, Y., Yao, Y., Lu, J., Pu, X., Hu, T., & Wang, P. (2020). Evaluation of the OPTRAM Model to retrieve soil moisture in the Sanjiang Plain of Northeast China. *Earth and Space Science, 7*, e2020EA001108

Dechesne, C., Lassalle, P., & Lefèvre, S. (2021). Bayesian Deep Learning with Monte Carlo Dropout for Qualification of Semantic Segmentation. In, *2021 IEEE International Geoscience and Remote Sensing Symposium IGARSS* (pp. 2536-2539): IEEE

den Besten, N., Dunne, S.S., Mahmud, A., Jackson, D., Aouizerats, B., de Jeu, R., Burger, R., Houborg, R., McGlinchey, M., & van der Zaag, P. (2023). Understanding Sentinel-1 backscatter response to sugarcane yield variability and waterlogging. *Remote sensing of environment, 290*, 113555

Domínguez-Niño, J.M., Oliver-Manera, J., Girona, J., & Casadesús, J. (2020). Differential irrigation scheduling by an automated algorithm of water balance tuned by capacitance-type soil moisture sensors. *Agricultural water management, 228*, 105880

Dubois, P.C., Van Zyl, J., & Engman, T. (1995). Measuring soil moisture with imaging radars. *IEEE Transactions on Geoscience and Remote Sensing, 33*, 915-926

Ebrahimi-Khusfi, M., Alavipanah, S.K., Hamzeh, S., Amiraslani, F., Samany, N.N., & Wigneron, J.-P. (2018). Comparison of soil moisture retrieval algorithms based on the synergy between SMAP and SMOS-IC. *International Journal of Applied Earth Observation and Geoinformation, 67*, 148-160

El Hajj, M., Baghdadi, N., Zribi, M., & Bazzi, H. (2017). Synergic use of Sentinel-1 and Sentinel-2 images for operational soil moisture mapping at high spatial resolution over agricultural areas. *Remote Sensing, 9*, 1292

El Hajj, M., Baghdadi, N., Zribi, M., Belaud, G., Cheviron, B., Courault, D., & Charron, F. (2016). Soil moisture retrieval over irrigated grassland using X-band SAR data. *Remote sensing of environment, 176*, 202-218

Entekhabi, D., Reichle, R.H., Koster, R.D., & Crow, W.T. (2010). Performance metrics for soil moisture retrievals and application requirements. *Journal of Hydrometeorology, 11*, 832-840

Fathololoumi, S., Vaezi, A.R., Alavipanah, S.K., Ghorbani, A., & Biswas, A. (2020). Comparison of spectral and spatial-based approaches for mapping the local variation of soil moisture in a semi-arid mountainous area. *Science of the total environment, 724*, 138319

Foroughi, H., Naseri, A.A., Boroomand Nasab, S., Hamzeh, S., Sadeghi, M., Tuller, M., & Jones, S.B. (2020). A new mathematical formulation for remote sensing of soil moisture based on the Red-NIR space. *International Journal of Remote Sensing, 41*, 8034-8047

Frison, P., Mougin, E., & Hiernaux, P. (1998). Observations and interpretation of seasonal ERS-1 wind scatterometer data over northern Sahel (Mali). *Remote sensing of environment, 63*, 233-242

Fung, A.K., Li, Z., & Chen, K.-S. (1992). Backscattering from a randomly rough dielectric surface. *IEEE Transactions on Geoscience and Remote Sensing, 30*, 356-369

Gao, B.-C. (1996). NDWI—A normalized difference water index for remote sensing of vegetation liquid water from space. *Remote sensing of environment, 58*, 257-266

Gao, L., Gao, Q., Zhang, H., Li, X., Chaubell, M.J., Ebtehaj, A., Shen, L., & Wigneron, J.-P. (2022). A deep neural network based SMAP soil moisture product. *Remote sensing of environment, 277*, 113059

Ge, L., Hang, R., Liu, Y., & Liu, Q. (2018). Comparing the performance of neural network and deep convolutional neural network in estimating soil moisture from satellite observations. *Remote Sensing, 10*, 1327

Ge, Y., Zhang, X., Atkinson, P.M., Stein, A., & Li, L. (2022). Geoscience-aware deep learning: A new paradigm for remote sensing. *Science of Remote Sensing, 5*, 100047
Grewal, M.S., & Andrews, A.P. (2014). *Kalman filtering: Theory and Practice with MATLAB*. John Wiley & Sons
Harfenmeister, K., Spengler, D., & Weltzien, C. (2019). Analyzing temporal and spatial characteristics of crop parameters using Sentinel-1 backscatter data. *Remote Sensing, 11*, 1569
Hassanpour, R., Zarehaghi, D., Neyshabouri, M.R., Feizizadeh, B., & Rahmati, M. (2020). Modification on optical trapezoid model for accurate estimation of soil moisture content in a maize growing field. *Journal of Applied Remote Sensing, 14*, 034519
Hu, Q., Yang, J., Xu, B., Huang, J., Memon, M.S., Yin, G., Zeng, Y., Zhao, J., & Liu, K. (2020). Evaluation of global decametric-resolution LAI, FAPAR and FVC estimates derived from Sentinel-2 imagery. *Remote Sensing, 12*, 912
Huete, A.R. (1988). A soil-adjusted vegetation index (SAVI). *Remote sensing of environment, 25*, 295-309
Khazaei, M., Hamzeh, S., Samani, N.N., Muhuri, A., Goïta, K., & Weng, Q. (2023). A web-based system for satellite-based high-resolution global soil moisture maps. *Computers & Geosciences, 170*, 105250
Kim, Y., & van Zyl, J.J. (2009). A time-series approach to estimate soil moisture using polarimetric radar data. *IEEE Transactions on Geoscience and Remote Sensing, 47*, 2519-2527
Lawrence, H., Wigneron, J.-P., Richaume, P., Novello, N., Grant, J., Mialon, A., Al Bitar, A., Merlin, O., Guyon, D., & Leroux, D. (2014). Comparison between SMOS Vegetation Optical Depth products and MODIS vegetation indices over crop zones of the USA. *Remote sensing of environment, 140*, 396-406
LeCun, Y., Bengio, Y., & Hinton, G. (2015). Deep learning. *nature, 521*, 436-444
Leimeister, J.M. (2010). Collective intelligence. *Business & Information Systems Engineering, 2*, 245-248
Leng, P., Yang, Z., Yan, Q.-Y., Shang, G.-F., Zhang, X., Han, X.-J., & Li, Z.-L. (2023). A framework for estimating all-weather fine resolution soil moisture from the integration of physics-based and machine learning-based algorithms. *Computers and Electronics in Agriculture, 206*, 107673
Li, Z.-L., Leng, P., Zhou, C., Chen, K.-S., Zhou, F.-C., & Shang, G.-F. (2021). Soil moisture retrieval from remote sensing measurements: Current knowledge and directions for the future. *Earth-Science Reviews, 218*, 103673
Liu, W., Wang, Z., Liu, X., Zeng, N., Liu, Y., & Alsaadi, F.E. (2017). A survey of deep neural network architectures and their applications. *Neurocomputing, 234*, 11-26
Liu, Y., Liu, Y., & Wang, W. (2019). Inter-comparison of satellite-retrieved and Global Land Data Assimilation System-simulated soil moisture datasets for global drought analysis. *Remote sensing of environment, 220*, 1-18
Ma, C., Johansen, K., & McCabe, M.F. (2022). Combining Sentinel-2 data with an optical-trapezoid approach to infer within-field soil moisture variability and monitor agricultural production stages. *Agricultural water management, 274*, 107942
Malone, T.W., Laubacher, R., & Dellarocas, C. (2009). Harnessing crowds: Mapping the genome of collective intelligence
Mananze, S., Pôças, I., & Cunha, M. (2019). Agricultural drought monitoring based on soil moisture derived from the optical trapezoid model in Mozambique. *Journal of Applied Remote Sensing, 13*, 024519
Marbach, D., Costello, J.C., Küffner, R., Vega, N.M., Prill, R.J., Camacho, D.M., Allison, K.R., Kellis, M., Collins, J.J., & Stolovitzky, G. (2012). Wisdom of crowds for robust gene network inference. *Nature methods, 9*, 796-804
Martínez-Fernández, J., González-Zamora, A., Sánchez, N., Gumuzzio, A., & Herrero-Jiménez, C. (2016). Satellite soil moisture for agricultural drought monitoring: Assessment of the SMOS derived Soil Water Deficit Index. *Remote sensing of environment, 177*, 277-286
Mattia, F., Le Toan, T., Picard, G., Posa, F.I., D'Alessio, A., Notarnicola, C., Gatti, A.M., Rinaldi, M., Satalino, G., & Pasquariello, G. (2003). Multitemporal C-band radar measurements on wheat fields. *IEEE Transactions on Geoscience and Remote Sensing, 41*, 1551-1560

Molijn, R.A., Iannini, L., Vieira Rocha, J., & Hanssen, R.F. (2019). Sugarcane productivity mapping through C-band and L-band SAR and optical satellite imagery. *Remote Sensing, 11*, 1109
Molinier, M., Miettinen, J., Ienco, D., Qiu, S., & Zhu, Z. (2021). Optical satellite image time series analysis for environment applications: From classical methods to deep learning and beyond. *Change Detection and Image Time Series Analysis 2: Supervised Methods*, 109-154
Moran, M.S., Peters-Lidard, C.D., Watts, J.M., & McElroy, S. (2004). Estimating soil moisture at the watershed scale with satellite-based radar and land surface models. *Canadian Journal of Remote Sensing, 30*, 805-826
Moskolaï, W.R., Abdou, W., & Dipanda, A. (2022). A Workflow for Collecting and Preprocessing Sentinel-1 Images for Time Series Prediction Suitable for Deep Learning Algorithms. *Geomatics, 2*, 435-456
Murphy, K.P. (2012). *Machine learning: a probabilistic perspective*. MIT press
Oh, Y. (2004). Quantitative retrieval of soil moisture content and surface roughness from multipolarized radar observations of bare soil surfaces. *IEEE Transactions on Geoscience and Remote Sensing, 42*, 596-601
Oh, Y., Sarabandi, K., & Ulaby, F.T. (1992). An empirical model and an inversion technique for radar scattering from bare soil surfaces. *IEEE Transactions on Geoscience and Remote Sensing, 30*, 370-381
Ouaadi, N., Ezzahar, J., Khabba, S., Er-Raki, S., Chakir, A., Ait Hssaine, B., Le Dantec, V., Rafi, Z., Beaumont, A., & Kasbani, M. (2021). C-band radar data and in situ measurements for the monitoring of wheat crops in a semi-arid area (center of Morocco). *Earth System Science Data, 13*, 3707-3731
Ouaadi, N., Jarlan, L., Ezzahar, J., Zribi, M., Khabba, S., Bouras, E., Bousbih, S., & Frison, P.-L. (2020). Monitoring of wheat crops using the backscattering coefficient and the interferometric coherence derived from Sentinel-1 in semi-arid areas. *Remote sensing of environment, 251*, 112050
Palmisano, D., Mattia, F., Balenzano, A., Satalino, G., Pierdicca, N., & Guarnieri, A.V.M. (2020). Sentinel-1 sensitivity to soil moisture at high incidence angle and the impact on retrieval over seasonal crops. *IEEE Transactions on Geoscience and Remote Sensing, 59*, 7308-7321
Paloscia, S., Santi, E., Fontanelli, G., Montomoli, F., Brogioni, M., Macelloni, G., Pampaloni, P., & Pettinato, S. (2014). The sensitivity of cosmo-skymed backscatter to agricultural crop type and vegetation parameters. *IEEE Journal Of Selected Topics In Applied Earth Observations And Remote Sensing, 7*, 2856-2868
Peng, J., Albergel, C., Balenzano, A., Brocca, L., Cartus, O., Cosh, M.H., Crow, W.T., Dabrowska-Zielinska, K., Dadson, S., & Davidson, M.W. (2021). A roadmap for high-resolution satellite soil moisture applications–confronting product characteristics with user requirements. *Remote sensing of environment, 252*, 112162
Petropoulos, G., Srivastava, P.K., Ferentinos, K.P., & Hristopoulos, D. (2020). Evaluating the capabilities of optical/TIR imaging sensing systems for quantifying soil water content. *Geocarto international, 35*, 494-511
Petropoulos, G.P., Ireland, G., & Barrett, B. (2015). Surface soil moisture retrievals from remote sensing: Current status, products & future trends. *Physics and Chemistry of the Earth, Parts A/B/C, 83*, 36-56
Pierdicca, N., Pulvirenti, L., & Bignami, C. (2010). Soil moisture estimation over vegetated terrains using multitemporal remote sensing data. *Remote sensing of environment, 114*, 440-448
Pipia, L., Muñoz-Marí, J., Amin, E., Belda, S., Camps-Valls, G., & Verrelst, J. (2019). Fusing optical and SAR time series for LAI gap filling with multioutput Gaussian processes. *Remote sensing of environment, 235*, 111452
Qi, J., Chehbouni, A., Huete, A.R., Kerr, Y.H., & Sorooshian, S. (1994). A modified soil adjusted vegetation index. *Remote sensing of environment, 48*, 119-126
Raissi, M., Perdikaris, P., & Karniadakis, G.E. (2019). Physics-informed neural networks: A deep learning framework for solving forward and inverse problems involving nonlinear partial differential equations. *Journal of Computational physics, 378*, 686-707
Rawat, K.S., Singh, S.K., & Pal, R.K. (2019). Synergetic methodology for estimation of soil moisture over agricultural area using Landsat-8 and Sentinel-1 satellite data. *Remote Sensing Applications: Society and Environment, 15*, 100250

Sadeghi, M., Babaeian, E., Tuller, M., & Jones, S.B. (2017). The optical trapezoid model: A novel approach to remote sensing of soil moisture applied to Sentinel-2 and Landsat-8 observations. *Remote sensing of environment, 198*, 52-68
Sadeghi, M., Jones, S.B., & Philpot, W.D. (2015). A linear physically-based model for remote sensing of soil moisture using short wave infrared bands. *Remote sensing of environment, 164*, 66-76
Santi, E., Paloscia, S., Pettinato, S., & Fontanelli, G. (2016). Application of artificial neural networks for the soil moisture retrieval from active and passive microwave spaceborne sensors. *International Journal of Applied Earth Observation and Geoinformation, 48*, 61-73
Singh, G., & Das, N.N. (2022). A data-driven approach using the remotely sensed soil moisture product to identify water-demand in agricultural regions. *Science of the total environment, 837*, 155893
Stumpf, M.P. (2020). Multi-model and network inference based on ensemble estimates: avoiding the madness of crowds. *Journal of the Royal Society Interface, 17*, 20200419
Surowiecki, J. (2005). *The wisdom of crowds*. Anchor
Tucker, C.J. (1979). Red and photographic infrared linear combinations for monitoring vegetation. *Remote sensing of environment, 8*, 127-150
Ulaby, F.T., Aslam, A., & Dobson, M.C. (1982). Effects of vegetation cover on the radar sensitivity to soil moisture. *IEEE Transactions on Geoscience and Remote Sensing*, 476-481
Ulaby, F.T., Sarabandi, K., Mcdonald, K., Whitt, M., & Dobson, M.C. (1990). Michigan microwave canopy scattering model. *International Journal of Remote Sensing, 11*, 1223-1253
Verhoest, N.E., Lievens, H., Wagner, W., Álvarez-Mozos, J., Moran, M.S., & Mattia, F. (2008). On the soil roughness parameterization problem in soil moisture retrieval of bare surfaces from synthetic aperture radar. *Sensors, 8*, 4213-4248
Villarroya-Carpio, A., Lopez-Sanchez, J.M., & Engdahl, M.E. (2022). Sentinel-1 interferometric coherence as a vegetation index for agriculture. *Remote sensing of environment, 280*, 113208
Wang, H., Mao, K., Yuan, Z., Shi, J., Cao, M., Qin, Z., Duan, S., & Tang, B. (2021a). A method for land surface temperature retrieval based on model-data-knowledge-driven and deep learning. *Remote sensing of environment, 265*, 112665
Wang, Q., Li, J., Jin, T., Chang, X., Zhu, Y., Li, Y., Sun, J., & Li, D. (2020). Comparative analysis of Landsat-8, Sentinel-2, and GF-1 data for retrieving soil moisture over wheat farmlands. *Remote Sensing, 12*, 2708
Wang, S., Li, R., Wu, Y., & Wang, W. (2023). Estimation of surface soil moisture by combining a structural equation model and an artificial neural network (SEM-ANN). *Science of the total environment, 876*, 162558
Wang, Z., Zhao, T., Qiu, J., Zhao, X., Li, R., & Wang, S. (2021b). Microwave-based vegetation descriptors in the parameterization of water cloud model at L-band for soil moisture retrieval over croplands. *GIScience & remote sensing, 58*, 48-67
Weiss, M., Baret, F., & Jay, S. (2020). S2ToolBox Level 2 products LAI, FAPAR, FCOVER. In: EMMAH-CAPTE, INRAe Avignon
Weiß, T., Ramsauer, T., Jagdhuber, T., Löw, A., & Marzahn, P. (2021). Sentinel-1 backscatter analysis and radiative transfer modeling of dense winter wheat time series. *Remote Sensing, 13*, 2320
Weiß, T., Ramsauer, T., Löw, A., & Marzahn, P. (2020). Evaluation of different radiative transfer models for microwave backscatter estimation of wheat fields. *Remote Sensing, 12*, 3037
Wu, S., Ren, J., Chen, Z., Yang, P., & Li, H. (2020). Soil moisture estimation based on the microwave scattering mechanism during different crop phenological periods in a winter wheat-producing region. *Journal of Hydrology, 590*, 125521
Xu, H. (2006). Modification of normalised difference water index (NDWI) to enhance open water features in remotely sensed imagery. *International Journal of Remote Sensing, 27*, 3025-3033
Yamashita, R., Nishio, M., Do, R.K.G., & Togashi, K. (2018). Convolutional neural networks: an overview and application in radiology. *Insights into imaging, 9*, 611-629
Yuan, Q., Shen, H., Li, T., Li, Z., Li, S., Jiang, Y., Xu, H., Tan, W., Yang, Q., & Wang, J. (2020). Deep learning in environmental remote sensing: Achievements and challenges. *Remote sensing of environment, 241*, 111716
Yuan, X., Li, H., Han, Y., Chen, J., & Chen, X. (2019). Monitoring of Sugarcane Crop based on Time Series of Sentinel-1 data: A case study of Fusui, Guangxi. In, *2019 8th International Conference on Agro-Geoinformatics (Agro-Geoinformatics)* (pp. 1-5): IEEE

Zeyliger, A., Muzalevskiy, K., Zinchenko, E., & Ermolaeva, O. (2022). Field test of the surface soil moisture mapping using Sentinel-1 radar data. *Science of the total environment, 807*, 151121
Zhang, D., & Zhou, G. (2016). Estimation of soil moisture from optical and thermal remote sensing: A review. *Sensors, 16*, 1308
Zhang, M., Lang, F., & Zheng, N. (2021). Soil moisture retrieval during the wheat growth cycle using SAR and optical satellite data. *Water, 13*, 135
Zhang, Y., Liang, S., Zhu, Z., Ma, H., & He, T. (2022). Soil moisture content retrieval from Landsat 8 data using ensemble learning. *ISPRS Journal of Photogrammetry and Remote Sensing, 185*, 32-47